

Article

Constraints on Ore Genesis from Trace Ore Mineralogy: A New Occurrence of Kupčikite and Padëraite from the Zhibula Cu Skarn Deposit, Southern Tibet

Jing Xu ^{1,*} , Cristiana Liana Ciobanu ², Nigel John Cook ² , Shen Gao ³, Taiping Zhao ⁴ and Jichen Jiang ¹¹ Zijin School of Geology and Mining, Fuzhou University, Fuzhou 350108, China; 13655071874@163.com² School of Chemical Engineering, The University of Adelaide, Adelaide, SA 5005, Australia; cristiana.ciobanu@adelaide.edu.au (C.L.C.); nigel.cook@adelaide.edu.au (N.J.C.)³ School of Earth Sciences and Resources, China University of Geosciences (Beijing), Beijing 100083, China; shen.gao@outlook.com⁴ Key Laboratory of Mineralogy and Metallogeny, Guangzhou Institute of Geochemistry, Chinese Academy of Sciences, Guangzhou 510640, China; tpzhao@gig.ac.cn

* Correspondence: xujing3800@126.com

Abstract: Mineral assemblages containing Cu-Bi sulfosalts, Bi chalcogenides, and Ag-(Au) tellurides have been identified in the mid-Miocene Zhibula Cu skarn deposit, Gangdese Belt, southern Tibet. Different mineral assemblages from three locations in the deposit, including proximal massive garnet skarn, proximal retrogressed pyroxene-dominant skarn in contact with marble, and distal banded garnet–pyroxene skarn hosted in marble, are studied to constrain the evolution of the mineralization. Hypogene bornite contains elevated Bi (mean 6.73 wt.%) and co-exists in proximal andradite skarn with a second bornite with far lower Bi content, carrollite, Au-Ag tellurides (hessite, petzite), and wittichenite. This assemblage indicates formation at relatively high temperatures (>400 °C) and high f_{S_2} and f_{Te_2} during prograde-stage mineralization. Assemblages of Bi sulfosalts (wittichenite, aikinite, kupčikite, and padëraite) and bismuth chalcogenides (e.g., tetradymite) in proximal pyroxene skarn are also indicative of formation at relatively high temperatures, but at relatively lower f_{Te_2} and f_{S_2} conditions. Within the reduced distal skarn (chalcopyrite–pyrrhotite-bearing) in marble, cobalt, and nickel occur as discrete minerals: cobaltite, melonite and cobaltic pentlandite. The trace ore mineral signature of the Zhibula skarn and the distributions of precious and critical trace elements such as Ag, Au, Co, Te, Se, and Bi support an evolving magmatic–hydrothermal system in which different parts of the deposit each define ore formation at distinct local physicochemical conditions. This is the first report of kupčikite and padëraite from a Chinese location. Their compositions are comparable to other occurrences, but conspicuously, they do not form nanoscale intergrowths with one another.

Keywords: ore mineralogy; Au-Ag tellurides; Bi chalcogenides; Cu-Bi sulfosalts; Zhibula Cu skarn; Tibet



Citation: Xu, J.; Ciobanu, C.L.; Cook, N.J.; Gao, S.; Zhao, T.; Jiang, J. Constraints on Ore Genesis from Trace Ore Mineralogy: A New Occurrence of Kupčikite and Padëraite from the Zhibula Cu Skarn Deposit, Southern Tibet. *Minerals* **2024**, *14*, 474. <https://doi.org/10.3390/min14050474>

Academic Editor: Giorgio Garuti

Received: 28 March 2024

Revised: 25 April 2024

Accepted: 26 April 2024

Published: 29 April 2024



Copyright: © 2024 by the authors. Licensee MDPI, Basel, Switzerland. This article is an open access article distributed under the terms and conditions of the Creative Commons Attribution (CC BY) license (<https://creativecommons.org/licenses/by/4.0/>).

1. Introduction

Copper skarns commonly contain anomalous concentrations of precious metals (Au and Ag) and may also be markedly enriched in one or more elements considered critical, including Co, Bi, Se, and Te [1]. This relative enrichment may be expressed by characteristic ore mineral assemblages that include a range of tellurides, selenides, and Bi-Pb and Cu-Bi sulfosalts. The presence of these minerals and their prevailing associations may provide valuable additional constraints on ore genesis, including estimates of the temperatures and pressures of ore-forming fluids, as well as relevant fugacities (e.g., f_{Se_2} , f_{S_2} , and f_{Te_2}) [2].

Telluride minerals are widespread in many types of ore deposits and can provide valuable physicochemical constraints on mineralization [2,3]. Tellurides have also been proposed as a tool to decipher orefield zonation in porphyry–epithermal systems, e.g., in

the Larga orefield, Romania [3]. Bismuth chalcogenides and some related tellurides when forming Bi-Te-bearing assemblages have low melting points and thus represent ideal melt scavengers that can play a significant role in gold enrichment processes [4].

Sulfosalts of the cuprobismutite homologous series are scarce in nature. The series includes cuprobismutite, hodrushite, and kupčikite, with the ideal formulae $\text{Cu}_8\text{AgBi}_{13}\text{S}_{24}$, $\text{Cu}_8\text{Bi}_{12}\text{S}_{22}$, and $\text{Cu}_8\text{Bi}_{10}\text{S}_{20}$, respectively ([5,6] and references therein). Paděraite, $\text{Cu}_6\text{AgPbBi}_{12}\text{S}_{22}$, is a closely related phase [7]. These minerals are reported from only a limited number of occurrences in mineralized veins and skarns, e.g., from the Felbertal metamorphic scheelite deposit, Austria [5,8]; the Băița Bihor Cu and Ocna de Fier Fe-Cu skarns, Romania [6,9]; the Swartberg rare metal pegmatite, South Africa [10]; and in Slovakia [11], Poland [12], and the high-grade Obari Au-Cu-Bi deposit, Japan [13]. Makovicky [14] postulated the general formula for these minerals as $\text{Cu}_4\text{Me}_{2(N-1)+1}\text{Bi}_4\text{S}_{2N+8}$, where Me is Bi and Ag, and N is the order number for each homologue type. However, subsequent study of natural samples revealed a greater compositional complexity due to substitutions of several other elements, notably Fe, Pb and Ag. The substitution mechanisms and site occupancies for these elements and the formation conditions of related species remain imperfectly constrained [9].

The Gangdese Belt, southern Tibet, hosts a large and growing number of ore deposits associated with episodes of magmatic activity spanning the Jurassic to Miocene (e.g., [15,16]). Porphyry Cu-Mo and Cu-Au deposits and associated skarns formed during this age range are the most economically significant types of mineralization. Until recently, there had been little detailed study of these deposits with respect to the distribution and ore mineralogy of minor components such as Co, Se, Bi, and Te [17,18]. This is despite the significance of such elements for interpretation of deposits related to magmatic–hydrothermal events. This contribution focuses on the occurrence of ore minerals and assemblages from the Zhibula Cu skarn that include several critical trace elements (Bi, Co, Te, Au, Ag, and Se). An appreciation of these minerals permits us to constrain the ore genesis of the deposit. Detailed mineral characterization also allows us to offer insights that may assist the potential recovery of these value-adding components.

2. Geological Setting

The Zhibula Cu skarn deposit has a reserve of 0.32 Mt Cu @ 1.64%. It is located approximately 2 km south of the Qulong porphyry Cu-Mo deposit in the Gangdese Belt, southern Tibet (Figure 1). Skarn orebodies occur as layers and less lenticular bodies within marble and tuffs of the 3 km-thick Yeba Formation, which has a U-Pb zircon age of 174.4 ± 1.7 Ma [19]. Skarn emplacement was controlled by the contacts between tuff and marble, as well as by fractures in the tuff. Outcropping intrusive rocks have not been identified in the mine area except for a few monzogranite and granodiorite dikes in deeper exploration drillholes. These granitoids have zircon U-Pb ages of ~17 Ma, which are concordant with those measured in minerals from the Qulong deposit [20]. Comparable molybdenite Re-Os ages (16–17 Ma; [21]) and zircon Hf-O isotopic signatures [22] for Zhibula and Qulong are also noted, strongly suggesting that skarns and porphyry mineralization share a common magmatic source and comprise a single large magmatic–hydrothermal ore system [22].

Isotope data for sulfur ($\delta^{34}\text{S}$ −0.1 to −6.8 ‰), hydrogen ($\delta\text{D}_{\text{H}_2\text{O}}$ −91 to −159 ‰), and oxygen ($\delta^{18}\text{O}_{\text{H}_2\text{O}}$ 1.5 to 9.2 ‰) further support an interpretation in which the Zhibula mineralization is related to magmatic–hydrothermal fluids. Fluid inclusion data confirm that ore-forming fluids changed from relatively high temperature and high salinity to low temperature, moderate salinity during transition from the prograde to retrograde stage [22].

Insights into skarn formation, particularly from the trace element signatures of garnet, were reported by Xu et al. [23]. Although minor endoskarn is noted in granodiorite, few skarns develop at the contacts between the Yeba Formation and granitoids. Instead, they typically occur within the Yeba Formation, with marble and tuff units as the dominant protoliths. A combination of different protoliths and variation in the local physicochemical

environment resulted in skarns of different appearance and composition, as well as the observed zonation at the orefield scale. Garnet is the dominant skarn mineral. The trace element endowment of garnet, particularly the rare earth element signatures, but also other elements (e.g., W, Sn, As, and Mo), changes in both space and time, as a function of multiple factors, e.g., mineralogy of co-crystallizing phases, variation in $X(\text{CO}_2)$, salinity, and proximity to local fluid sources.

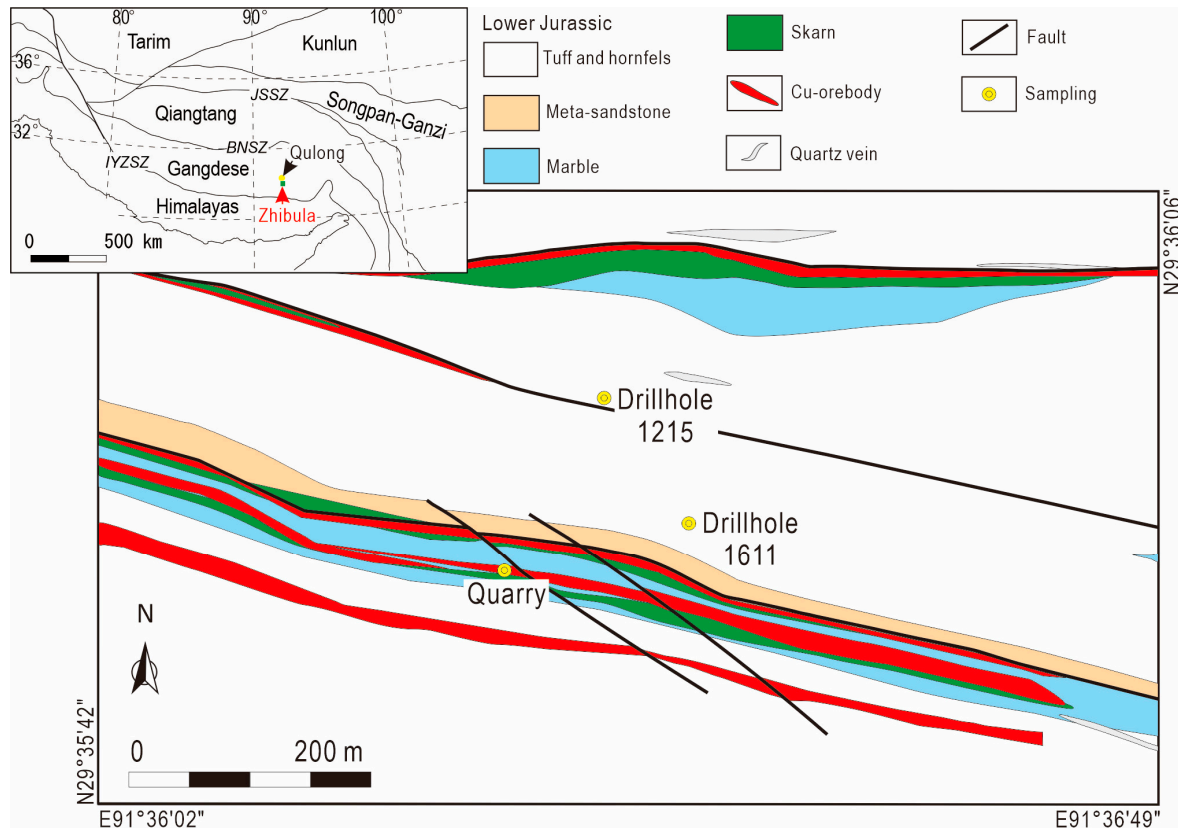


Figure 1. Simplified geological map of the Zhibula Cu skarn deposit, modified after Xu et al. [22]. Abbreviations: JSSZ—Jinsha Suture Zone; BNSZ—Bangong–Nujiang Suture Zone; IYZSZ—Indus–Yarlung Zangbo Suture Zone.

Copper skarns are primarily comprised of chalcopyrite and bornite. Other trace ore minerals include magnetite, sphalerite, galena, scheelite, molybdenite, Cu–Bi sulfosalts, Bi chalcogenides, and Au–Ag tellurides. Solid solution between scheelite and powellite (up to 80 mol.% powellite) is considered the retrogressed product of the replacement of garnet. A detailed micro- to nanoscale study of scheelite–powellite aggregates showed that non-linear thermodynamics governing the patterning in non-ideal solid solution may account for the formation of distinct patterning domains within the Mo-rich areas of the aggregates. The sharpest contrast in chemical composition of the Mo-rich scheelite is also recognizable by variation in the growth directions [24].

3. Sampling and Analytical Methodology

Detailed skarn mineralogy and associated mineralization has been depicted by Xu et al. [23]. We focus on three types of mineralized skarn here: distal banded garnet–pyroxene skarn in marble (e.g., sample 321), proximal massive garnet skarn (e.g., sample 374), and proximal retrogressed pyroxene-dominated skarn (e.g., sample 180). For locations and short descriptions of these samples, the reader is referred to Figure 1 and Table 1.

Table 1. Overview of samples studied.

Skarn Type	Sample ID	Drill Hole	Depth (m)	Main Skarn Assemblage							Minor Skarn Assemblage	Ore Minerals		
				Grt	Px	Czo	Act	Chl	Qz	Cal		Sulfides	Oxides	
Distal skarn (banded Grt-Px in marble)	321	1611	321	xx	x	x				x	xxx	Wo, Ap, Ttn, Ves	Pyh, Ccp, Gn, Sp, Pn	
	323	1611	323	xx	x					x	xxx	Wo, Ap, An, Ves	Pyh, Ccp, Gn, Sp, Pn	
Proximal skarn (massive Grt)	372	1611	372	xxx	x		x	x	x	x		Ap	Ccp, Bn, Mol, Cli, Gn, Sp, Py	Mag, Hem, Sch
	374	1611	374	xxx	x		x		x	x		Ap	Ccp, Bn, Cc, Sp, Gn, Ptz, Hes, Wtc, Cli	
	8	quarry	-	xxx	x			x	x	x		Ap	Bn, Ccp, Mol, Cc, Gn, Hes, Ptz, El, Cli	Sch
Proximal skarn (retrogressed Px in contact with marble)	180	1611	180	x	xxxx	x		x	xx	xxx		Ap, Wo	Ccp, Bn, Wtc, Aik, Ttd, Pde, Kup	Mag, Hem, Sch
	355	1215	355	x	xx	xxx	xx	xx	xxx	xx		Ap	Ccp, Sp, Gn	

Abbreviations: Act—actinolite; Aik—aikinite; An—anorthite; Ap—apatite; Bn—bornite; Cal—calcite; Cc—chalcocite; Ccp—chalcopyrite; Chl—chlorite; Cli—carrollite; Czo—clinozoisite; El—electrum; Gn—galena; Hem—hematite; Hes—hessite; Kup—kupčikite; Mag—magnetite; Mol—molybdenite; Pde—padéraite; Ptz—petzite; Pwl—powellite; Px—pyroxene; Py—pyrite; Pyh—pyrrhotite; Qz—quartz; Sp—sphalerite; Ttd—tetradymite; Ttn—titanite; Ves—vesuvianite; Wo—wollastonite; Wtc—wittichenite. xxx—major; xx—minor; x—trace.

Samples were prepared as 1 inch-diameter polished blocks and thin sections. All analytical work was performed at Adelaide Microscopy, University of Adelaide. Imaging was performed in reflected light and using an FEI Quanta 450 scanning electron microscope (SEM) (FEI, Hillsboro, OR, USA) equipped with energy-dispersive X-ray spectrometry and backscatter electron (BSE) imaging capabilities. BSE imaging was performed at a 20 kV accelerating voltage and 10 nA beam current. Quantitative mineral compositional data was obtained on a Cameca SX-Five electron probe microanalyzer (EPMA) (Cameca Instruments Inc., Fitchburg, WI, USA) and a Resonetics M-50-LR 193-nm Excimer laser microprobe (Resonetics, Nashua, NH, USA) coupled with an Agilent 7700cx quadrupole ICP-MS (LA-ICP-MS) (Agilent, Santa Clara, CA, USA).

Foils for nanoscale study were prepared using an FEI-Helios nanoLab (FEI, Hillsboro, OR, USA) focused ion beam—scanning electron microscopy (FIB—SEM). Transmission electron microscopy (TEM) imaging and selected area electron diffraction (SAED) patterns were obtained using a Philips CM200 microscope (Amsterdam, The Netherlands), equipped with a LaB6 source and Gatan Orius digital camera (Gatan Inc., Pleasanton, CA, USA), and operated at 200 kV. Data processing was carried out using DigitalMicrograph™ 3.11.1 (Gatan Inc., Pleasanton, CA, USA) software for indexation of electron diffractions. High-angle annular dark-field scanning transmission electron microscopy (HAADF STEM) studies were performed using an FEI Titan Themis (FEI, Hillsboro, OR, USA). TIA software (v4.7.2) was used for STEM image processing. WinWulff© (JCrystalSoft, Livermore, CA, USA) was used to index diffraction patterns. CrystalMaker® (v10.5.7) (CrystalMaker Software Ltd., Kidlington, UK) was used to generate crystal structure models, and image simulations were created using STEM for xHREMTM software (v 4.1) (HREM Research, Tokyo, Japan).

4. Results

4.1. Ore Petrography and Mineralogy

Minor sulfides, chalcopyrite associated with pyrrhotite, occur in the distal skarn formed within altered marble with a weak banding expressed by different proportions of grossular (Gr_{~50}) and diopside (Di_{~80}) (Figure 2a). In contrast, the proximal skarn represented by massive andradite garnet skarn is typified by the presence of chalcopy-

rite and bornite, as well as subordinate Au-Ag-Bi-Te and Co minerals, which occur as disseminations and/or larger patches (Figure 2b,c), as well as veinlets.

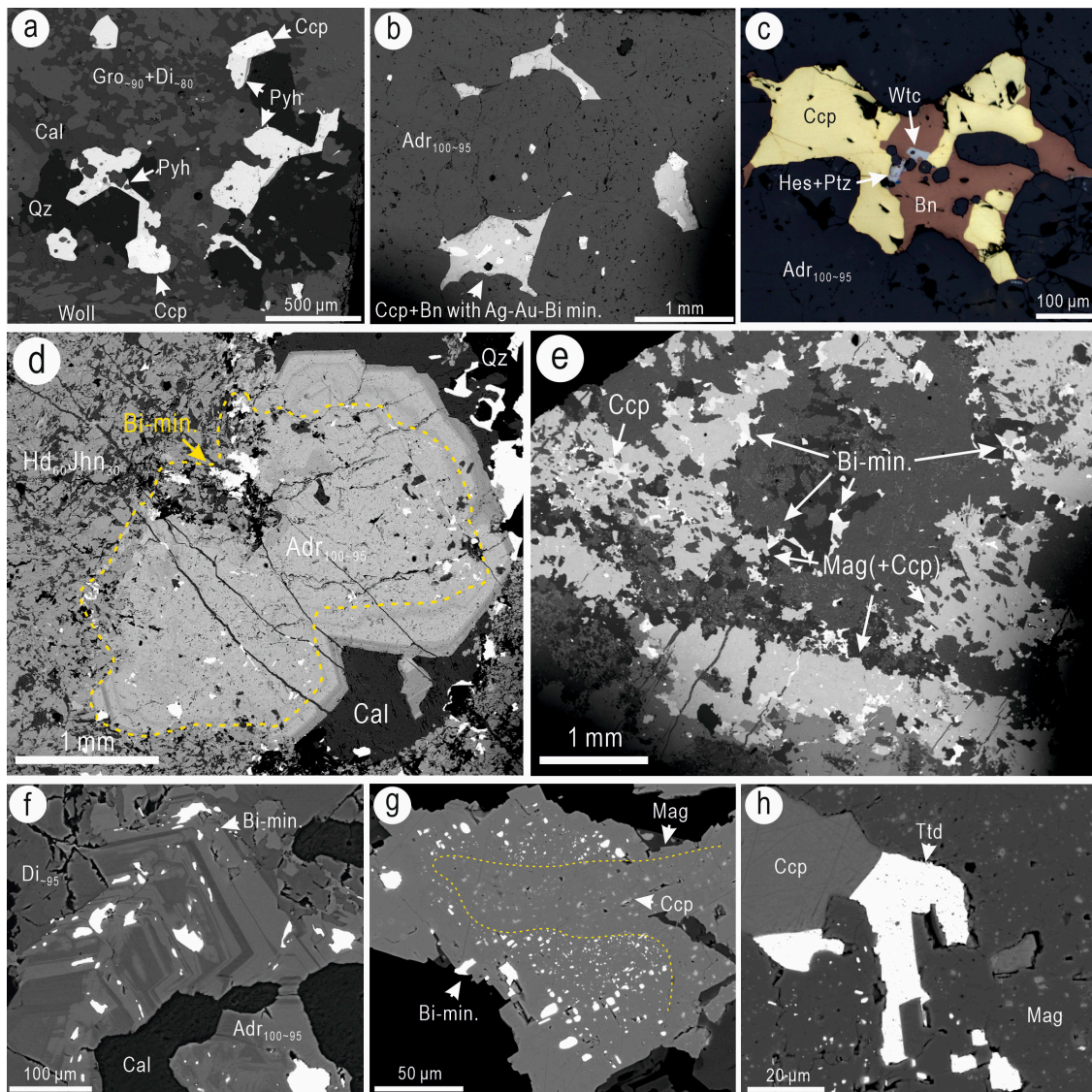


Figure 2. Representative photomicrographs showing skarn and ore mineral associations in the Zhibula skarn. (a) Chalcopyrite–pyrrhotite associated with quartz replaces an assemblage of grossular (Gro_{-90}), diopside (Di_{-80}), and wollastonite in the distal banded skarn within marble (sample 321). (b,c) Intergranular chalcopyrite–bornite associated with Ag–Au–Bi minerals in proximal massive andradite (Adr_{100-95}) garnet skarn (sample 374). (d) Replacement of andradite (Adr_{100-95}) by hedenbergite–johannsenite ($Hd_{60}Jhn_{30}$) and Bi-bearing minerals in proximal retrogressed pyroxene-dominant skarn (sample 180). (e) Abundant magnetite together with disseminations of Cu–Fe sulfides (chalcopyrite) and Bi-bearing minerals in hedenbergite–johannsenite skarn (sample 180). (f–h) Details showing extensive replacement of garnet and magnetite by Bi-bearing minerals (sample 180). Note the abundant pores in magnetite, which represent evidence of replacement. Abbreviations: Adr—andradite; Bn—bornite; Cal—calcite; Ccp—chalcopyrite; Di—diopside; Gro—grossular; Hd—hedenbergite; Jhn—johannsenite; Mag—magnetite; Pyh—pyrrhotite; Qz—quartz; Ttd—tetradymite. All are BSE images except for (b) (reflected polarized).

Bismuth sulfosalts and tellurides are most abundant throughout the proximal pyroxene-dominant, garnet skarn that experienced strong retrogression marked by changes from Mg–pyroxene (diopside) to Mn- and Fe-rich pyroxene (johannsenite–hedenbergite) and re-

placement of andradite (Figure 2d). Bismuth minerals occur as tiny inclusions in the garnet or as larger patches along the contact between the two silicates. The same Bi minerals are also abundant in areas with higher concentrations of magnetite (Figure 2e). Chalcopyrite is also present throughout the magnetite. In detail, zoned garnet shows reworking of smaller particles of Bi minerals along the zones, into coarser patches, and across zones (Figure 2f). Magnetite also displays abundant Bi minerals within growth zones, outside from grain cores that are mottled with inclusions of chalcopyrite (Figure 2g). Coarser, euhedral tetradymite ($\text{Bi}_2\text{Te}_2\text{S}$) occurs at contacts between chalcopyrite and magnetite (Figure 2h).

Distal skarn pyrrhotite occurs together with chalcopyrite within calcite (Figure 3a). In detail, inclusions of diopside are noted within the sulfides (Figure 3b). Pentlandite is present as minor lamellae within pyrrhotite (Figure 3b). Note the flame-like morphology of pentlandite indicative of exsolution from solid solution (Figure 3c). Trace sphalerite and seleniferous galena (clausthalite?) are also noted along the margins or within pyrrhotite (Figure 3d,e).

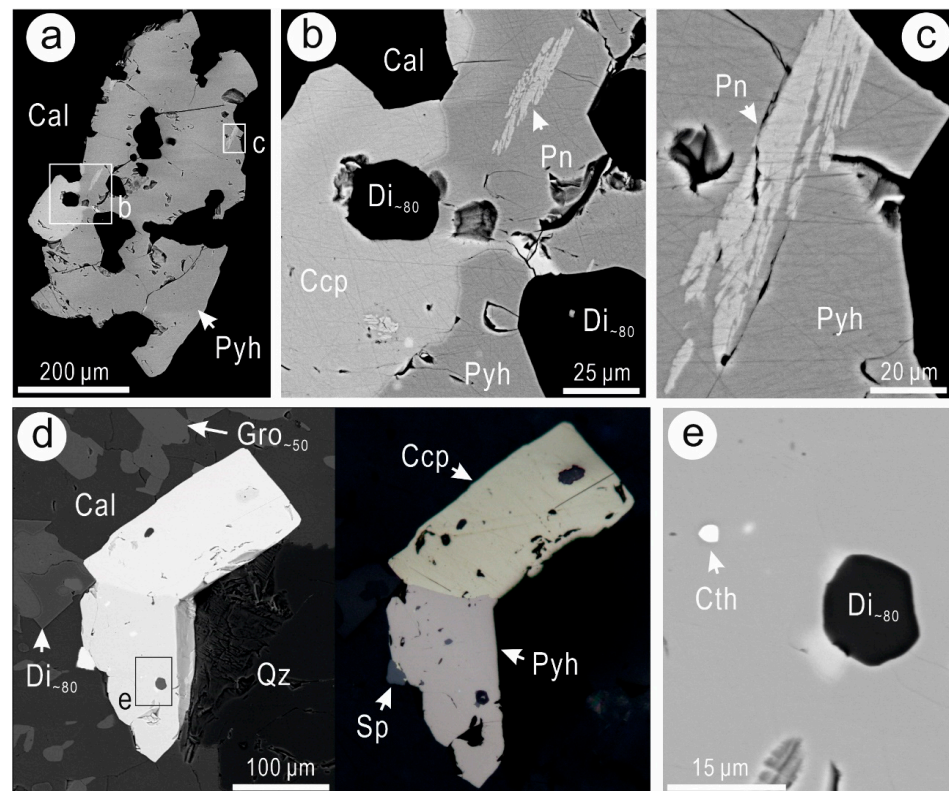


Figure 3. Representative images showing ore mineral associations in distal banded garnet–pyroxene skarn. (a–c) Pyrrhotite co-existing with chalcopyrite; diopside is enclosed in pyrrhotite. Details show lamellar pentlandite exsolution in pyrrhotite. (d,e) Chalcopyrite formed together with pyrrhotite; note micron-scale seleniferous galena and diopside enclosed in pyrrhotite. All are BSE images except right panel on d (reflected polarized). Abbreviations: Cal—calcite; Ccp—chalcopyrite; Cth—clausthalite or seleniferous galena; Di—diopside; Pn—pentlandite; Pyh—pyrrhotite; Qz—quartz; Sp—sphalerite.

In the proximal garnet skarn, carrollite (CuCo_2S_4) accompanies bornite (Figure 4a–c) and is the only confirmed cobalt mineral. Locally, carrollite is replaced by late chalcocite and trace galena (Figure 4a). Marginal or grain boundary replacement of bornite by lamellar chalcocite is noted (Figure 4b,c). Bornite occurs as blebs within chalcopyrite. Particularly interesting are binary blebs of bornite and a Bi-rich bornite-like phase containing ~6.7 wt.% Bi that appears brighter on BSE images and has a light reddish-brown color in reflected light (Figure 4d–f).

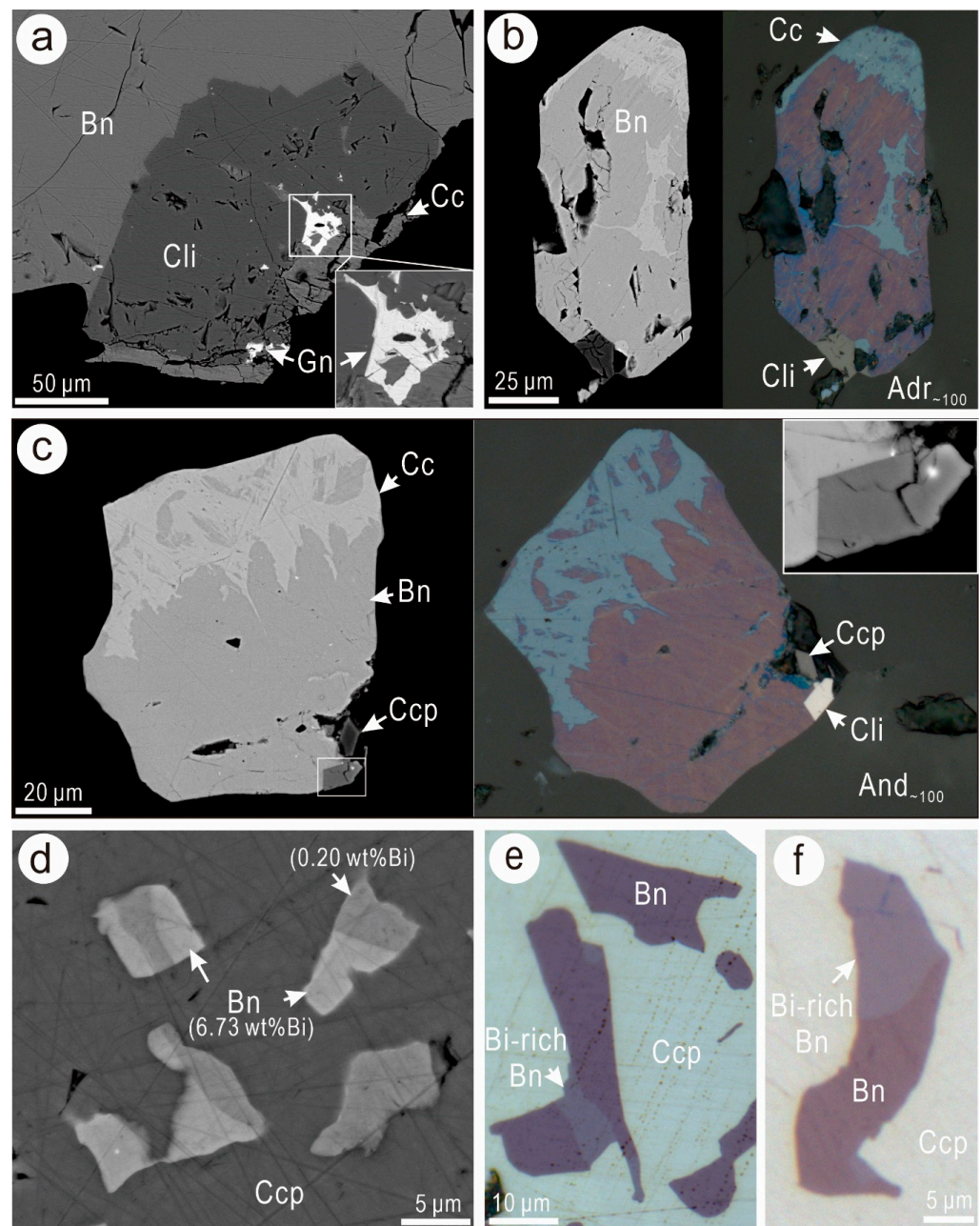


Figure 4. Representative images showing ore mineral associations in proximal massive garnet skarn. (a) Bornite co-exists with carrollite; both are altered by late chalcocite and galena. (b,c) Relatively coarse-grained bornite replaced by late chalcocite. Note the presence of trace carrollite along margins of bornite. (d) Fine-grained bornite exsolved from chalcopyrite. (d–f) Co-existing bornite phases (high and low Bi) occurring as inclusions within chalcopyrite. Note the lighter reddish-brown color in Bi-rich bornite compared to normal bornite. All images are BSE images except the right part of b and c, e, and f, which are reflected polarized photomicrographs. Abbreviations: Adr—andalusite; Bn—bornite; Cc—chalcocite; Ccp—chalcopyrite; Cli—carrollite; Gn—galena.

Abundant tiny Ag–Au tellurides and the common Cu–Bi sulfosalt wittichenite (Cu_3BiS_3) are observed as inclusions within Cu–(Fe) sulfides from the proximal garnet skarn (Figure 5). The Ag–Au tellurides are dominated by hessite (Ag_2Te) with subordinate petzite (Ag_3AuTe_2) and electrum (Au,Ag). Hessite, generally accompanied by petzite, displays a close relationship with bornite and wittichenite (Figure 5a–c), and locally is associated with molybdenite. Rare melonite (NiTe_2), together with tsumoite (BiTe), and hessite were also observed within

wittichenite (Figure 5d). Minor sphalerite and galena together with Ag-Au-Bi minerals can form along the margin of bornite grains (Figure 5e–f). Notable is the presence of petzite and hessite as filaments and patchy inclusions within wittichenite (Figure 5f).

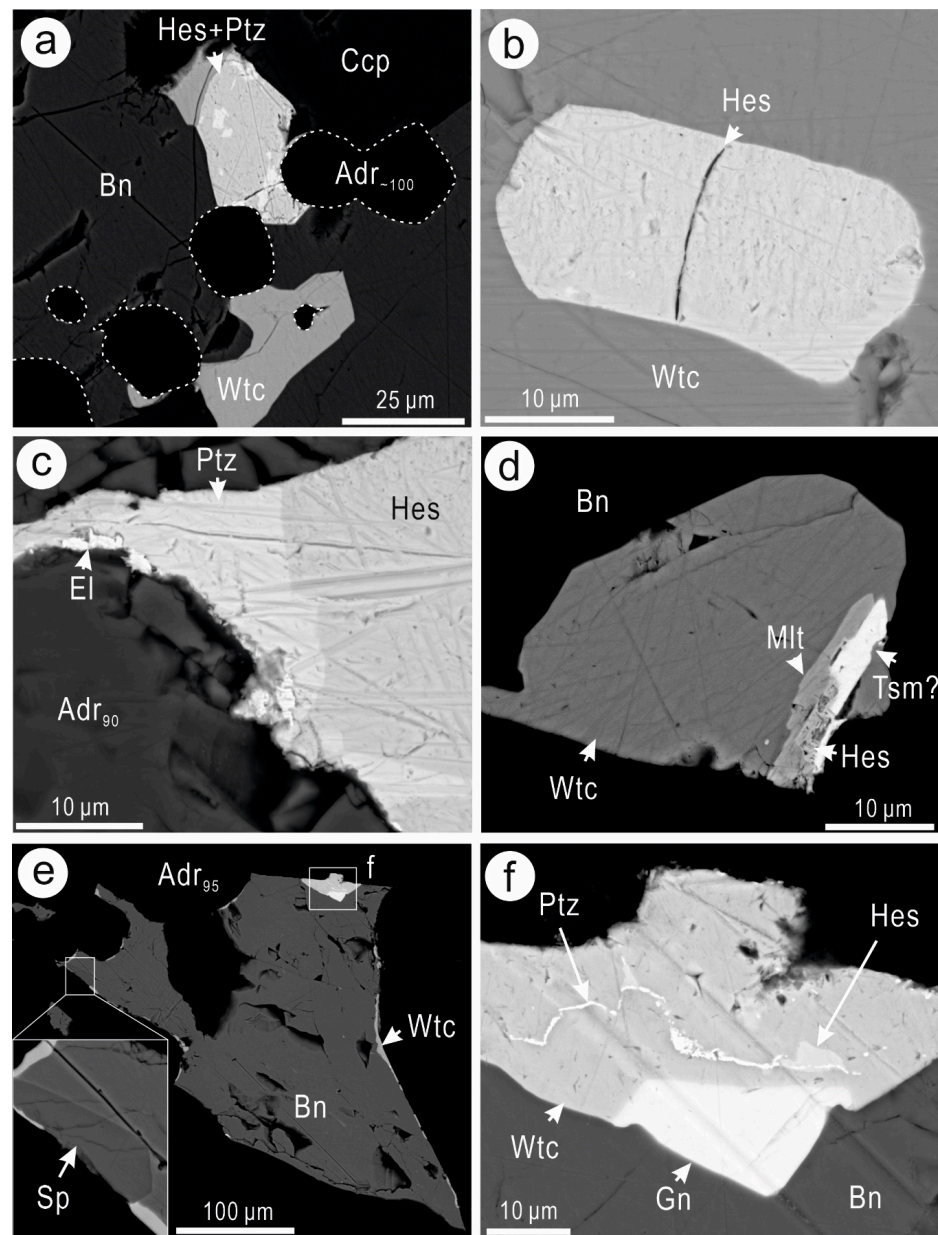


Figure 5. Representative BSE images showing Ag-Au-Bi mineral assemblages in proximal massive garnet skarn. (a) Trace petzite in hessite together with coarser grains of bornite, wittichenite and chalcopyrite. (b) Hessite inclusion in wittichenite. (c) Trace electrum occurs along the margin of petzite and hessite. (d) Minor melonite co-existing with hessite and tsumoite in wittichenite and bornite. (e) Minor sphalerite, galena, and wittichenite at margins of bornite. (f) Detail of (e) showing trace hessite and petzite. Abbreviations: Adr—andradite; Bn—bornite; Ccp—chalcopyrite; El—electrum; Gn—galena; Hes—hessite; Mlt—melonite; Tsm—tsumoite; Ptz—petzite; Sp—sphalerite; Wtc—wittichenite.

In the proximal retrogressed pyroxene skarn, the main Bi minerals are wittichenite and aikinite (CuPbBiS_3) (Figure 6). These phases occur together at contacts between chalcopyrite and magnetite (Figure 6a). Dense fields of micron- to submicron-scale lamellae of tetradymite form inner parts of the wittichenite enclosed in magnetite (Figure 6b). These

textures are likely indicative of tetradymite exsolution from a broad wittichenite solid solution. Wittichenite and aikinite form along magnetite margins; adjacent tetradymite is present as a separate, coarser (~50 μm -long) lamella (Figure 6c,d). Such textural relationships indicate co-crystallization between the two Bi minerals and their host magnetite and chalcopyrite.

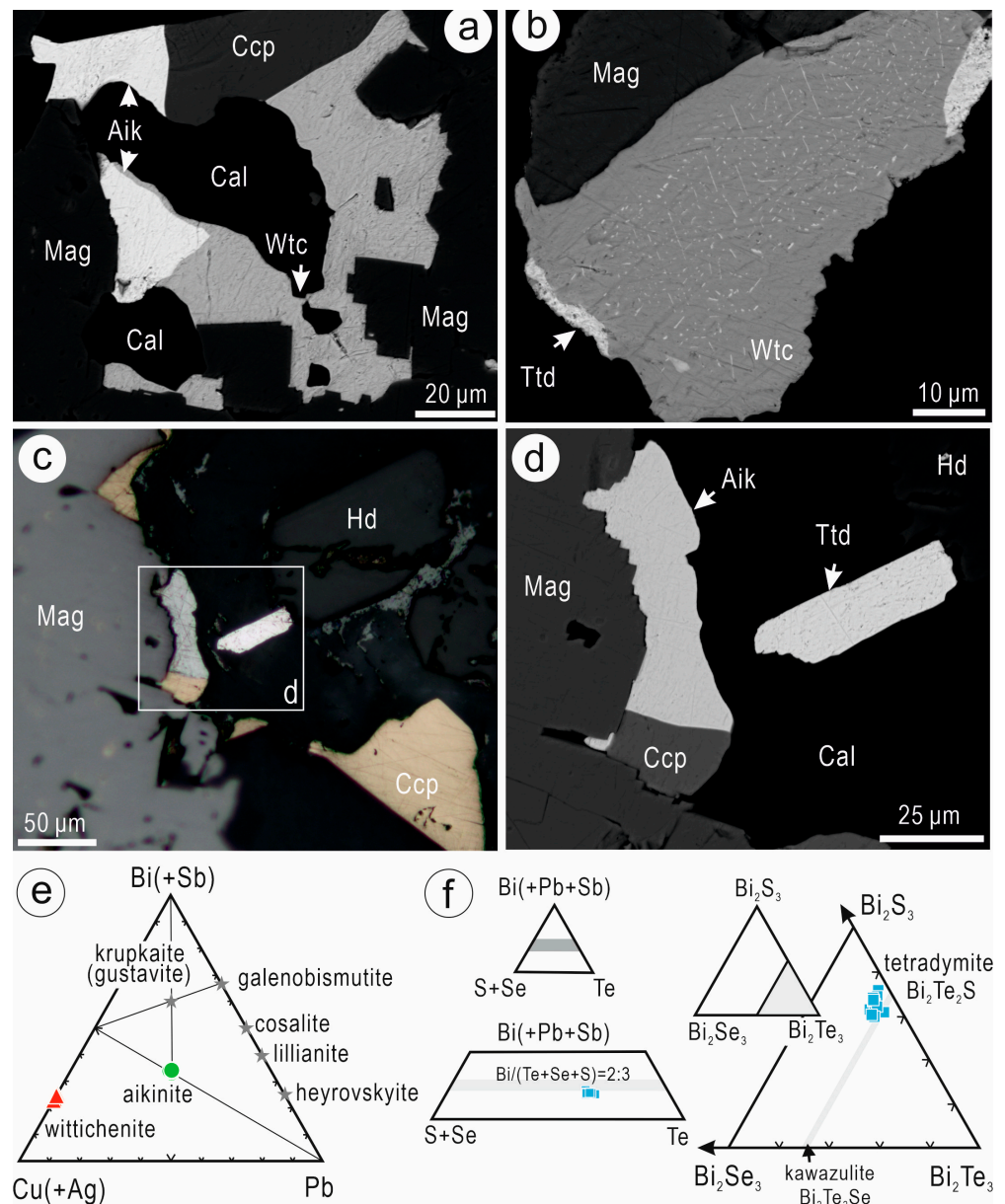


Figure 6. Representative images showing Bi-bearing mineral associations in proximal retrogressed pyroxene-dominated skarn (a–d) and their composition plots (e,f) (after [3]). (a) Co-existing wittichenite, aikinite, chalcopyrite and calcite. (b) Exsolution of lamellar tetradymite from wittichenite. (c,d) Granular aikinite and tetradymite associated with chalcopyrite. All are BSE images except c (reflected polarized). Abbreviations: Adr—andalusite; Aik—aikinite; Cal—calcite; Ccp—chalcopyrite; Hed—hedenbergite; Mag—magnetite; Ttd—tetradymite; Wtc—wittichenite.

4.2. Padérite and Kupčikite: Micron to Nanoscale Characterization

Two rare Bi-Cu-(Pb) sulfosalts, kupčikite and padérite, are observed within the retrogressed skarn enriched in associations of Bi minerals (Figure 7). The two rare sulfosalts occur as discrete grains, oriented at $\sim 90^\circ$ to one another at the edge of a larger lamella of tetradymite (Figure 7a). Padérite is euhedral, whereas kupčikite is marginally replaced by

wittichenite (Figure 7b). This also displays a scalloped boundary with tetradymite. Padëraite is also replaced by wittichenite, as observed from marginal relationships (Figure 7c). Slightly ragged boundaries between the two sulfosalts are also observed (Figure 7d). Tetradymite is present as a small sigmoid-shaped inclusion on the boundary of padëraite, whereas wittichenite is observed on the side of the kupčikite. Taken together, these textural relationships indicate reworking of primary padëraite–kupčikite + tetradymite associations (Figure 7a,b) with superimposed replacement by wittichenite (Figure 7c,d).

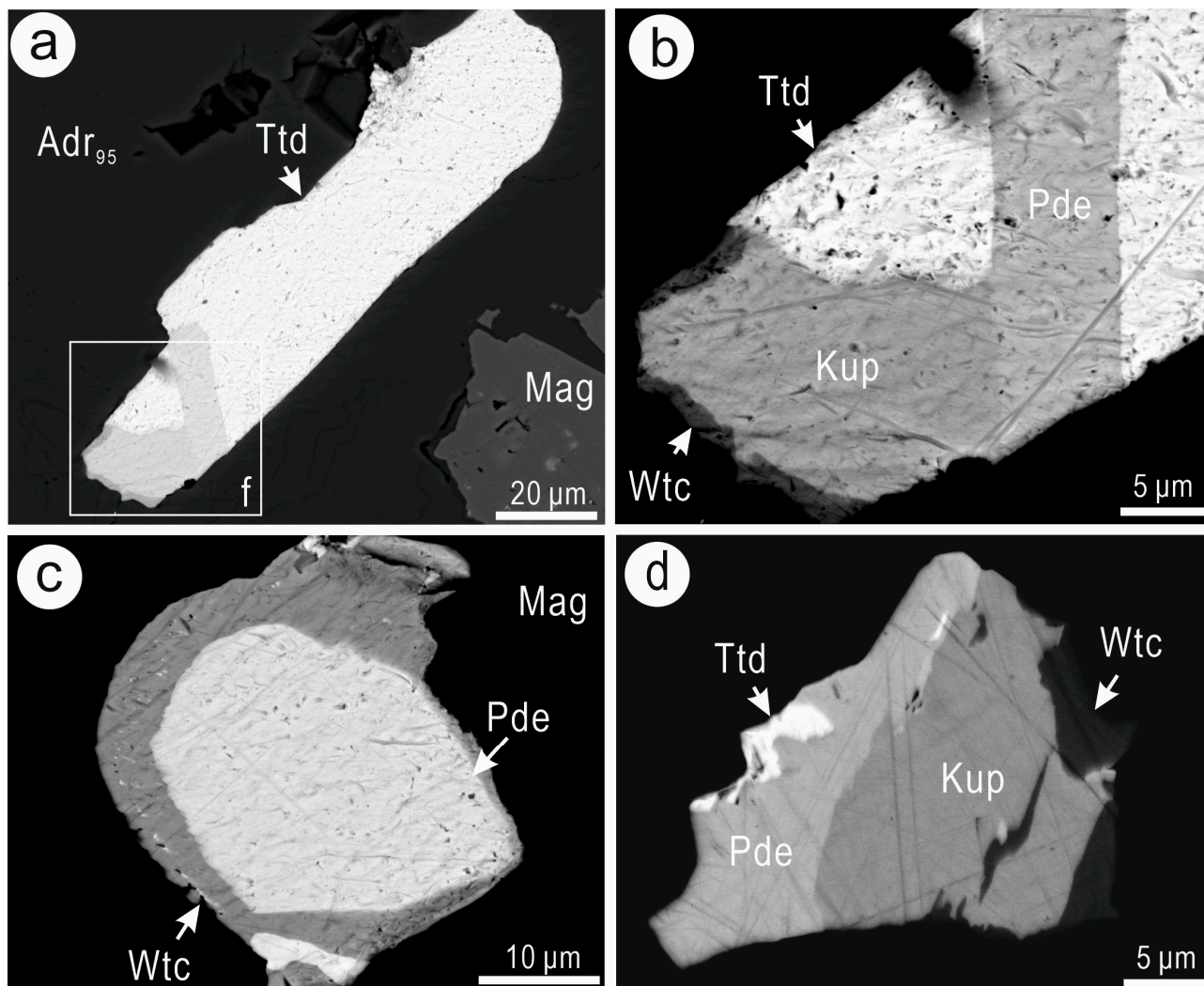


Figure 7. BSE images showing padëraite and kupčikite associations in proximal retrogressed pyroxene-dominated skarn. (a,b) Intergrowths between padëraite and kupčikite together with tetradymite. (c) Padëraite surrounded by wittichenite and magnetite. (d) Co-existing padëraite, kupčikite, and tetradymite, which were replaced by wittichenite. Abbreviations: Adr—andradite; Kup—kupčikite; Mag—magnetite; Pde—padëraite; Ttd—tetradymite; Wtc—wittichenite.

Nanoscale study was carried out on several S/TEM foils to assess the identity of the two rare sulfosalts (Figure 8). Two of these foils comprise kupčikite with a rim of wittichenite towards the boundary with magnetite at depth (Figure 8a) and padëraite alone (Figure 8b). The [010] zone axis was targeted in both sulfosalts, as this is the best orientation to assess their crystal-structure building modules using HR TEM [6].

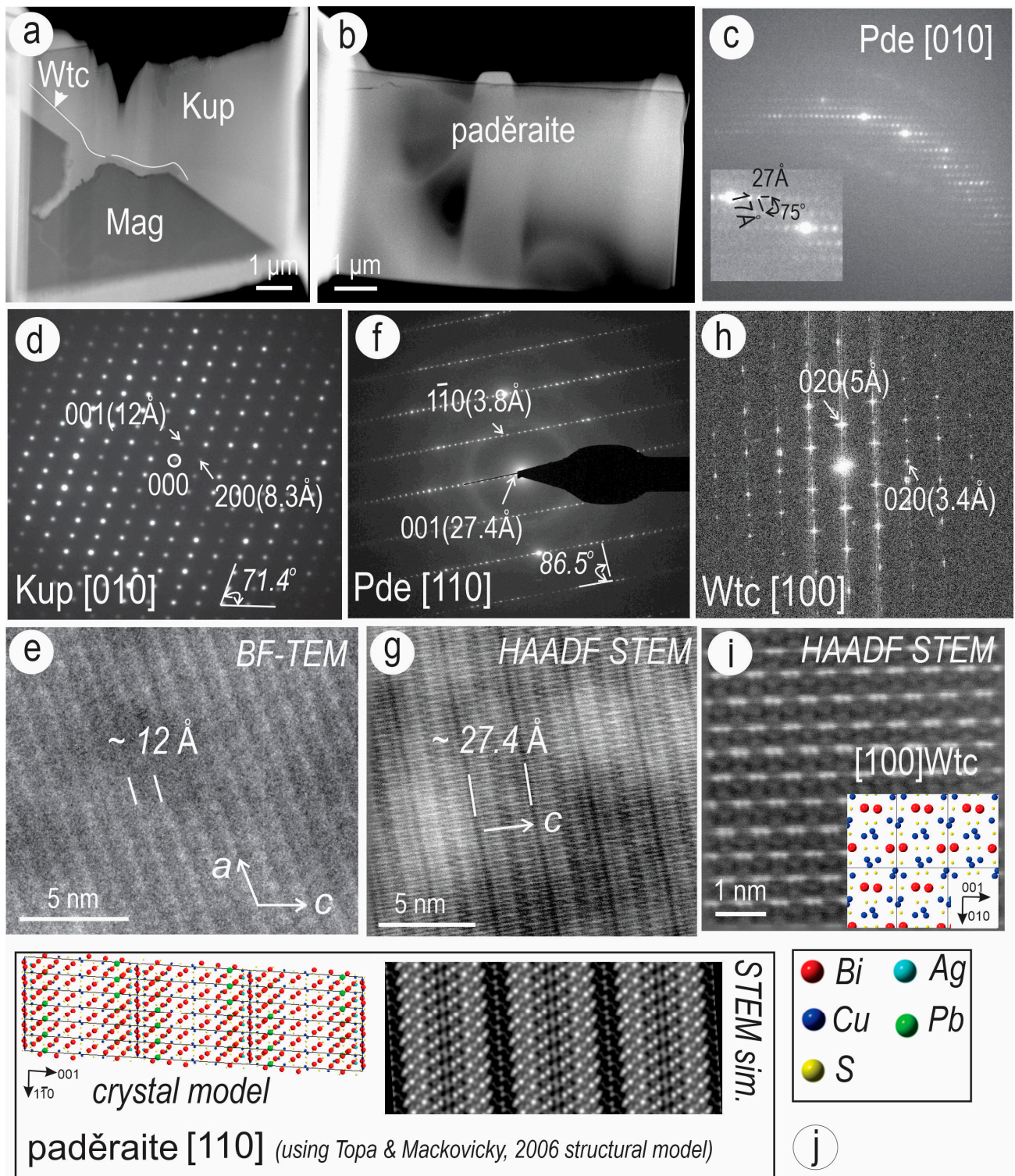


Figure 8. (a,b) Overview of S/TEM foils studied for kupčikite (Kup) and paděraite (Pad). (c) Selected area electron diffraction (SAED) showing measurements of 27 Å and 17 Å between lattice vectors at 75° indicative of paderaitite tilted close to [010] zone axis. (d–g) SAED patterns and corresponding images representative of kupčikite (d,e) and paděraite (f,g) tilted on zone axes as labeled. The images show 12 Å and 27 Å repeats corresponding to the *c* parameter of kupčikite and paderaitite, respectively. BF-TEM—bright-field transmission electron microscopy; HAADF STEM—high-angle annular dark-

field scanning transmission electron microscopy. (h,i) Fast Fourier transform and image of wittichenite (Wtc) tilted on zone axis as labeled. Crystal model of wittichenite on the same [100] zone axis as an overlay on the image in (i) showing the bismuth atoms as dumbbell arrays on the HAADF STEM image. (j) Crystal model and STEM simulation for padëraite on the [110] zone axis. Note the correspondence with the HAADF STEM image in (g) is the simulation for padëraite on the [110] zone axis. Abbreviations: Kup—kupčikite; Mag—magnetite; Pde—padëraite; Wtc—wittichenite.

Padëraite from a third foil was tilted only close to [010], as shown in the selected area electron diffraction (SAED) in Figure 8c, but could not be imaged. Kupčikite from the foil in Figure 8a was identified from the SAED on the [010] zone axis (Figure 8d). This could be imaged only in BF-TEM mode (Figure 8e) as this zone axis was out of reach for the tilt allowed on the S/TEM microscope. The BF-TEM image shows regular ~ 12 Å repeats corresponding to the *c* parameter of kupčikite (indexing using Topa et al. [8]). Padëraite from the foil in Figure 8b was identified from the SAED and HAADF STEM imaging on the [110] zone axis (Figure 8f,g). The image shows regular ~ 27 Å repeats corresponding to the *c* parameter of padëraite using one of the structures of Topa and Makovicky [25]. Wittichenite was also identified from SAED and HAADF STEM imaging on the [100] zone axis (Figure 8h,i). The crystal structure model for wittichenite (overlay on image in Figure 8i) and crystal model and STEM simulation for padëraite on the [110] zone axis (Figure 8j) show a good match with the images.

4.3. Compositional Data

4.3.1. EPMA Data

EPMA data for the Bi-rich bornite, Cu-Bi sulfosalts, Bi chalcogenides, and Au-Ag tellurides are listed in Tables 2–6. Data for other sulfides are given in Tables S1–S7.

Our EPMA dataset indicates that most bornite is stoichiometric Cu_5FeS_4 , albeit with detectable levels of Bi (mean 0.20 wt.%), Ag (mean 0.12 wt.%), Co (~ 0.17 wt.%), and Se (~ 0.09 wt.%) (Table 2). The Bi-rich bornite-like phase occurring in sample 374 (Figure 4d–f) is relatively Fe-rich, Cu-poor, and contains a mean Bi content of 6.73 wt.%, giving the empirical composition $\text{Cu}_{4.37}\text{Bi}_{0.16}\text{Fe}_{1.28}\text{S}_{4.18}$ (Table 2). Both chalcopyrite ($\text{Cu}_{0.98-1.02}\text{Fe}_{0.98-1.01}\text{S}_{1.97-2.01}$) and chalcocite ($\text{Cu}_{1.85}\text{Fe}_{0.06}\text{S}_{1.09}$) are stoichiometric and host comparable contents of Bi (0.06–0.16 wt.%), Ag ($<dl \sim 0.16$ wt.%), Se ($<dl \sim 0.08$ wt.%) and Co ($<dl \sim 0.10$ wt.%) (Table S1).

Compositional data for all Cu-Bi-(Pb) sulfosalts are listed in Tables 3 and 4 and plotted in Figure 6e (wittichenite and aikinite) and Figure 9 (kupčikite and padëraite).

Wittichenite ($\text{Cu}_{2.92-2.99}\text{Fe}_{0.03-0.07}\text{Bi}_{0.91-0.96}\text{S}_{3.00-3.06}$) and aikinite ($\text{Cu}_{1.05}\text{Fe}_{0.04}\text{Pb}_{1.06}\text{Bi}_{1.10}\text{S}_{3.16}$) contain detectable Fe (average contents 0.77 wt.% and 0.53 wt.%, respectively). Selenium contents are also quite high in both wittichenite (0.05–1.04 wt.%) and aikinite (0.32–1.07 wt.%). Tellurium concentrations are below minimum limits of detection in both minerals. Wittichenite contains measurable Ag concentrations in some analyses ($<dl \sim 0.50$ wt.%), whereas Ag is below the minimum detection limit in all analyzed aikinites.

Kupčikite is a scarce mineral with fewer than 10 localities noted to date. Analytical data for kupčikite (Table 4) give the empirical formula $(\text{Cu}_{3.43}\text{Fe}_{0.59})_{4.02}(\text{Bi}_{4.96}\text{Pb}_{0.02}\text{Cd}_{0.03}\text{Ag}_{0.01})_{5.02}(\text{S}_{9.82}\text{Se}_{0.14})_{9.96}$ ($n = 18$). Iron (1.34–2.53 wt.%) is an essential component in kupčikite. Kupčikite displays variable contents of Pb ($<dl$ to 0.68 wt.%), but Cd (0.06–0.34 wt.%) is relatively steady. Kupčikite also contains relatively high, consistent concentrations of Se (0.60–0.79 wt.%), but no Te.

Padëraite contains Pb (average 7.23 wt.%), Ag (average 0.26 wt.%), Cd (average 0.07 wt.%) and minor Fe (average 0.50 wt.%). It also has Se contents (average 0.99 wt.%) that are comparable with kupčikite: and trace amounts of Te (average 0.16 wt.%). Analysis of padëraite gives the empirical formula $\text{Cu}_7(\text{Cu}_{0.05}\text{Ag}_{0.09}\text{Fe}_{0.34}\text{Pb}_{1.31}\text{Cd}_{0.02}\text{Bi}_{11.10})_{12.91}(\text{S}_{21.56}\text{Se}_{0.47}\text{Te}_{0.05})_{22.08}$ ($n = 12$; Table 4).

Table 2. Summary EPMA data for Bi-rich and normal bornite in the Zhibula Cu skarn.

	Bi-Rich Bornite-like Phase (wt.%)								Normal Bornite (wt.%)											
	Sample 374 (n = 3)				Sample 374 (n = 13)				Sample 8 (n = 29)				Sample 180 (n = 3)				Sample 372 (n = 2)			
	1	2	3	Mean	Max.	Min.	SD	Mean	Max.	Min.	SD	Mean	Max.	Min.	SD	Mean	Max.	Min.	SD	Mean
Cu	54.6	55.24	54.77	54.87	64.50	61.39	0.73	63.55	63.90	62.50	0.37	63.35	60.86	60.59	0.11	60.71	62.93	62.52	0.20	62.72
Ag	0.09	0.09	0.07	0.08	0.20	<dl	0.06	0.03	0.23	<dl	0.04	0.12	0.06	<dl	0.00	0.02	0.10	0.09	0.00	0.10
Fe	14.53	14.12	13.68	14.11	11.59	10.27	0.31	11.31	11.48	10.78	0.17	11.19	15.23	14.76	0.20	14.96	11.65	11.64	0.00	11.64
Pb	<dl	0.07	<dl	0.02	0.10	<dl	0.02	0.04	0.25	<dl	0.05	0.05	<dl	<dl	-	<dl	0.09	<dl	0.03	0.05
Bi	6.47	6.82	6.9	6.73	0.51	0.12	0.10	0.20	0.31	0.11	0.04	0.18	0.30	0.25	0.02	0.27	0.39	0.25	0.07	0.32
Co	26.6	26.5	26.32	0.01	0.03	<dl	0.01	0.01	0.04	<dl	0.01	0.01	0.17	0.08	0.04	0.14	0.02	<dl	0.01	0.01
S	0.07	0.07	0.09	26.47	25.64	23.38	0.51	25.02	27.74	25.77	0.35	26.35	26.83	26.22	0.27	26.60	26.23	26.13	0.05	26.18
Se	<dl	0.02	0.02	0.08	0.09	<dl	0.01	0.04	0.09	<dl	0.02	0.03	0.05	<dl	0.00	0.02	0.06	<dl	0.02	0.03
Total	102.35	102.91	101.83	102.36	101.14	98.59	0.74	100.22	102.08	99.91	0.62	101.27	102.61	102.52	0.04	102.58	101.34	100.77	0.28	101.06
Formula (to 10 atoms)																				
Cu	4.336	4.383	4.391	4.370	5.167	4.938	0.058	5.038	4.978	4.820	0.031	4.931	4.672	4.632	0.017	4.650	4.901	4.894	0.004	4.898
Ag	0.004	0.004	0.004	0.004	0.009	-	0.003	0.002	0.011	-	0.002	0.005	0.003	-	0.000	0.001	0.005	0.004	0.000	0.004
Pb	-	0.002	-	0.001	0.002	-	0.001	0.001	0.006	-	0.001	0.001	-	-	-	-	0.002	-	0.000	0.001
Fe	1.313	1.275	1.248	1.279	1.058	0.926	0.029	1.020	1.009	0.950	0.012	0.991	1.331	1.286	0.020	1.303	1.037	1.032	0.002	1.035
Bi	0.156	0.165	0.168	0.163	0.012	0.003	0.002	0.005	0.007	0.003	0.001	0.004	0.007	0.006	0.000	0.006	0.009	0.006	0.002	0.008
Total M	5.809	5.828	5.811	5.816	6.232	5.998	0.055	6.065	5.991	5.779	0.037	5.933	6.010	5.934	0.035	5.960	5.946	5.945	0.001	5.945
S	4.186	4.167	4.183	4.179	3.997	3.768	0.054	3.932	4.221	4.006	0.038	4.065	4.066	3.990	0.034	4.039	4.055	4.050	0.003	4.053
Se	0.004	0.005	0.006	0.005	0.006	-	0.001	0.003	0.006	-	0.001	0.002	0.003	-	0.000	0.001	0.004	-	0.000	0.002
S(+Se)	4.191	4.172	4.189	4.184	4.002	3.768	0.055	3.935	4.221	4.009	0.037	4.067	4.066	3.990	0.035	4.040	4.055	4.054	0.001	4.055
M/S	1.386	1.397	1.387	1.390	1.654	1.499	0.037	1.542	1.495	1.369	0.022	1.459	1.506	1.460	0.022	1.476	1.467	1.466	0.001	1.466

Note: <dl, below minimum limit of detection. For detailed data, see Table S1.

Table 3. Summary EPMA data for common Cu-Bi sulfosalts (wittichenite and aikinite) in the Zhibula Cu skarn.

	Wittichenite (Sample 374, n = 4)				Wittichenite (Sample 180, n = 10)				Aikinite (Sample 180, n = 11)			
	Max.	Min.	SD	Mean	Max.	Min.	SD	Mean	Max.	Min.	SD	Mean
Cu	39.80	38.79	0.38	39.35	38.03	36.88	0.39	38.00	10.98	10.54	0.13	10.75
Ag	0.50	0.30	0.07	0.39	0.22	<dl	0.05	0.19	<dl	<dl	-	<dl
Fe	1.16	0.60	0.22	0.83	0.87	0.54	0.14	0.77	0.86	0.07	0.29	0.53
Cd	0.09	0.06	0.01	0.08	0.06	0.04	0.01	0.04	0.14	0.05	0.04	0.04
Pb	<dl	<dl	-	<dl	<dl	<dl	-	<dl	36.22	35.11	0.37	35.53
Mn	<dl	<dl	-	<dl	0.08	<dl	0.02	0.02	0.03	<dl	0.01	0.01
Bi	40.42	39.15	0.51	39.55	41.89	40.57	0.44	40.90	37.56	36.07	0.46	37.01
S	20.12	19.80	0.12	19.94	20.45	19.39	0.30	20.06	16.91	15.70	0.39	16.25
Te	<dl	<dl	-	<dl	<dl	<dl	-	<dl	0.02	<dl	0.01	0.01
Se	0.11	<dl	0.02	0.07	1.04	0.09	0.25	0.26	1.07	0.32	0.29	0.67
Total	101.44	98.97	0.98	100.18	101.45	98.41	0.87	99.87	102.11	99.59	0.91	100.64
	Formula (to 7 atoms)						Formula (to 6 atoms)					
Cu	3.004	2.977	0.011	2.989	2.922	2.870	0.016	2.923	1.157	0.947	0.078	1.050
Ag	0.022	0.013	0.003	0.017	0.010	-	0.002	0.009	-	-	-	-
Pb	-	-	-	-	-	-	-	-	1.185	0.978	0.080	1.064
Fe	0.100	0.053	0.018	0.072	0.075	0.047	0.012	0.033	0.101	0.008	0.033	0.041
Cd	0.004	0.003	0.001	0.003	0.003	0.002	0.000	0.002	0.008	0.003	0.002	0.002
Cu+Ag+Fe	3.126	3.047	0.029	3.078	2.986	2.875	0.031	2.965	1.202	1.007	0.075	1.091
Pb+Cd	0.004	0.003	0.001	0.003	0.003	0.002	0.000	0.002	1.188	0.984	0.081	1.066
Bi	0.925	0.904	0.008	0.914	0.989	0.959	0.011	0.957	1.204	1.010	0.084	1.099
Bi+Sb+As	0.925	0.904	0.008	0.914	0.989	0.959	0.011	0.957	1.204	1.010	0.084	1.099
Total M	4.034	3.968	0.026	3.994	3.947	3.867	0.023	3.924	3.549	3.022	0.235	3.256
S	3.028	2.963	0.025	3.002	3.120	2.988	0.035	3.060	3.470	2.871	0.264	3.145
Te	-	-	-	-	-	-	-	-	0.001	-	0.000	0.001
Se	0.007	-	0.001	0.005	0.065	0.006	0.015	0.016	0.092	0.027	0.024	0.053
S(+Te+Se)	3.032	2.966	0.026	3.006	3.133	3.053	0.023	3.076	3.507	2.943	0.264	3.198
Charge M	5.946	5.850	0.042	5.896	5.922	5.808	0.037	5.874	7.145	6.071	0.478	6.562
Charge S	6.063	5.932	0.051	6.012	6.266	6.106	0.046	6.152	7.014	5.885	0.528	6.396
mean	5.965	5.939	0.011	5.954	6.057	6.014	0.013	6.013	7.037	6.005	0.502	6.479
diff.	0.014	-0.204	0.091	-0.116	-0.185	-0.437	0.079	-0.278	0.292	0.004	0.087	0.166
diff (%)	0.2	-3.4	1.5	-1.9	-3.1	-7.2	1.3	-4.6	4.8	0.1	1.5	2.6

Note: <dl, below minimum limit of detection. For detailed data, see Table S2.

Table 4. Summary EPMA data for trace Cu-Bi sulfosalts (kupčikite and paděraite) in the Zhibula Cu skarn (sample 180).

	Pb	Bi	Cu	Ag	Fe	Cd	S	Se	Te	Total	Pb	Bi	Ag	Cu	Fe	Cd	S	Se	Te	eV%
	Kupčikite										Formula (to 19 atoms)									
Ku-1	0.46	64.90	13.33	0.21	2.33	0.23	19.81	0.63	<dl	101.9	0.035	4.941	0.031	3.337	0.664	0.033	9.832	0.127	-	-1.3
Ku-2	0.52	64.37	13.09	0.19	2.14	0.29	19.72	0.65	<dl	100.97	0.040	4.949	0.028	3.310	0.616	0.041	9.883	0.132	-	-2.3
Ku-3	0.26	64.17	13.39	0.11	2.00	0.27	19.57	0.68	<dl	100.45	0.020	4.956	0.016	3.400	0.578	0.039	9.851	0.139	-	-2.1
Ku-4	<dl	64.22	13.08	0.13	2.19	0.34	19.66	0.70	<dl	100.32	-	4.954	0.019	3.318	0.632	0.049	9.885	0.143	-	-2.5
Ku-5	0.21	64.21	13.73	0.19	2.17	0.26	19.61	0.64	<dl	101.02	0.016	4.918	0.028	3.458	0.622	0.037	9.791	0.130	-	-1.3
Ku-6	<dl	63.82	13.52	<dl	2.32	0.20	19.45	0.71	<dl	100.02	-	4.929	-	3.434	0.671	0.029	9.792	0.145	-	-1.3
Ku-7	0.39	63.95	13.68	0.15	2.26	0.22	19.77	0.63	<dl	101.05	0.030	4.879	0.022	3.432	0.645	0.031	9.832	0.127	-	-2.1
Ku-8	0.04	64.06	13.54	0.14	2.21	0.22	19.67	0.60	<dl	100.48	0.003	4.920	0.021	3.420	0.635	0.031	9.848	0.122	-	-2.0
Ku-9	<dl	64.39	13.35	0.09	2.34	0.26	19.46	0.68	<dl	100.57	-	4.966	0.013	3.386	0.675	0.037	9.783	0.139	-	-0.6
Ku-10	<dl	64.21	13.70	0.08	2.53	0.10	19.71	0.70	<dl	101.03	-	4.892	0.012	3.432	0.721	0.014	9.788	0.141	-	-1.4
Ku-11	0.23	64.64	13.23	<dl	2.39	0.12	19.57	0.75	<dl	100.93	0.018	4.970	-	3.345	0.688	0.017	9.809	0.153	-	-1.1
Ku-12	0.51	63.34	13.27	<dl	1.94	0.06	19.34	0.63	<dl	99.09	0.040	4.961	-	3.418	0.569	0.009	9.873	0.131	-	-2.4
180Ku-13	0.77	63.99	13.45	<dl	1.76	0.11	18.98	0.79	<dl	99.85	0.061	5.032	-	3.478	0.518	0.016	9.730	0.164	-	-0.1
Ku-14	0.68	63.30	13.69	<dl	1.51	0.14	18.90	0.77	<dl	98.99	0.054	5.008	-	3.562	0.447	0.021	9.747	0.161	-	-0.9
Ku-15	0.06	63.09	13.41	0.13	1.34	0.08	18.85	0.72	<dl	97.68	0.005	5.048	0.020	3.529	0.401	0.012	9.832	0.152	-	-2.2
Ku-16	0.85	63.77	13.79	<dl	1.51	0.17	19.32	0.79	<dl	100.2	0.067	4.966	-	3.532	0.440	0.025	9.808	0.163	-	-2.3
Ku-17	0.08	63.29	13.07	0.10	1.93	0.11	18.92	0.70	<dl	98.2	0.006	5.028	0.015	3.415	0.574	0.016	9.798	0.147	-	-0.9
Ku-18	0.14	64.28	13.99	<dl	1.97	0.09	19.67	0.72	<dl	100.86	0.011	4.923	-	3.523	0.565	0.013	9.820	0.146	-	-2.3
Min.	<dl	63.09	13.07	<dl	1.34	0.06	18.85	0.60	<dl	97.68	-	4.879	-	3.310	0.401	0.009	9.730	0.122	-	-2.5
Max.	0.85	64.90	13.99	0.21	2.53	0.34	19.81	0.79	<dl	101.90	0.067	5.048	0.031	3.562	0.721	0.049	9.885	0.164	-	-0.1

Table 4. Cont.

	Pb	Bi	Cu	Ag	Fe	Cd	S	Se	Te	Total	Pb	Bi	Ag	Cu	Fe	Cd	S	Se	Te	eV%
Mean	0.29	64.00	13.46	0.08	2.05	0.18	19.44	0.69		100.20	0.02	4.96	0.01	3.43	0.59	0.03	9.82	0.14		−1.6
SD	0.26	0.48	0.26	0.04	0.32	0.08	0.31	0.06		1.05	0.02	0.05	0.01	0.07	0.09	0.01	0.04	0.01		0.7
	Padëraite										Formula (to 42 atoms)									
Pad-1	7.25	62.26	11.48	0.36	0.51	0.12	18.64	0.98	0.13	101.73	1.310	11.153	0.125	6.762	0.342	0.040	21.765	0.465	0.038	−1.8
Pad-2	7.29	61.92	11.58	0.28	0.39	0.05	18.57	0.96	0.18	101.22	1.324	11.146	0.098	6.855	0.263	0.017	21.789	0.457	0.053	−2.3
Pad-3	7.58	61.70	11.66	0.30	0.38	0.09	18.31	1.02	0.19	101.23	1.383	11.159	0.105	6.935	0.257	0.030	21.586	0.488	0.056	−0.9
Pad-4	7.35	61.07	11.35	0.27	0.68	0.09	18.32	1.09	0.15	100.37	1.344	11.075	0.095	6.769	0.461	0.030	21.657	0.523	0.045	−1.6
Pad-5	7.25	61.87	11.36	0.25	0.47	0.09	18.08	1.01	0.16	100.54	1.337	11.311	0.089	6.829	0.322	0.031	21.546	0.489	0.048	0.1
Pad-6	7.58	61.76	11.16	0.24	0.47	0.12	18.48	0.98	0.22	101.01	1.384	11.182	0.084	6.645	0.318	0.040	21.811	0.470	0.065	−2.1
Pad-7	7.12	61.70	11.20	0.25	1.09	0.07	18.06	0.99	0.08	100.56	1.306	11.224	0.088	6.700	0.742	0.024	21.415	0.477	0.024	1.7
Pad-8	6.92	61.91	12.87	0.21	0.50	<dl	18.14	0.92	0.18	101.65	1.250	11.090	0.073	7.581	0.335	-	21.181	0.436	0.053	1.7
Pad-9	6.85	61.93	12.47	0.25	0.27	<dl	18.45	0.97	0.16	101.35	1.238	11.095	0.087	7.347	0.181	-	21.546	0.460	0.047	−1.3
Pad-10	7.37	61.15	12.80	0.11	0.39	0.06	18.64	0.97	0.16	101.65	1.319	10.846	0.038	7.466	0.259	0.020	21.551	0.455	0.046	−2.0
Pad-11	7.26	61.15	12.44	0.28	0.45	0.05	18.45	0.96	0.16	101.20	1.310	10.940	0.097	7.318	0.301	0.017	21.515	0.455	0.047	−1.2
Pad-12	6.93	61.22	12.56	0.29	0.42	0.11	18.18	1.02	0.19	100.92	1.258	11.018	0.101	7.433	0.283	0.037	21.328	0.486	0.056	0.0
Min.	6.85	61.07	11.16	0.11	0.27	<dl	18.06	0.92	0.08	100.37	1.238	10.846	0.038	6.645	0.181	-	21.181	0.436	0.024	−2.3
Max.	7.58	62.26	12.87	0.36	1.09	0.12	18.64	1.09	0.22	101.73	1.384	11.311	0.125	7.581	0.742	0.040	21.811	0.523	0.065	1.7
Mean	7.23	61.64	11.91	0.26	0.50	0.07	18.36	0.99	0.16	101.12	1.314	11.103	0.090	7.053	0.339	0.024	21.558	0.472	0.048	−0.8
SD	0.23	0.37	0.63	0.06	0.20	0.03	0.20	0.04	0.03	0.44	0.045	0.120	0.020	0.330	0.137	0.009	0.180	0.022	0.010	1.3

Note: <dl, below minimum limit of detection.

Table 5. Summary EPMA data for Bi chalcogenides in the Zhibula Cu skarn.

	Cu	Ag	Cd	Pb	Bi	S	Te	Se	Total	Cu	Ag	Pb	Cd	Cu+Ag	Pb+Cd	Bi	Total M	S	Te	Se	S(+Te+Se)
	Tetradymite (sample 180, n = 15)										Formula (to 5 atoms)										
Max.	0.13	0.22	0.14	0.13	59.51	5.05	37.21	2.17	101.65	0.015	0.014	0.004	0.009	0.022	0.009	1.971	1.983	1.090	2.012	0.191	3.077
Min.	<dl	<dl	<dl	<dl	56.83	4.16	34.33	0.74	98.51	-	-	-	-	-	-	1.910	1.923	0.917	1.862	0.065	3.017
SD	0.02	0.04	0.03	0.03	0.73	0.28	0.80	0.40	0.99	0.003	0.003	0.001	0.002	0.005	0.002	0.014	0.014	0.052	0.042	0.036	0.014
Mean	0.08	0.06	0.04	0.05	58.39	4.69	35.48	1.44	100.24	0.009	0.004	0.002	0.003	0.012	0.004	1.928	1.945	1.010	1.919	0.126	3.055

Note: <dl, below minimum limit of detection. For detailed data, see Table S3.

Table 6. Summary EPMA data for Au-Ag tellurides in the Zhibula Cu skarn.

	S	Se	Cu	Ag	Hg	Te	Bi	Au	Total	S	Se	Te	S+Se+Te	Cu	Ag	Hg	Bi	Au	Total M	
	Hessite (sample 8, n = 7)										Formula (to 3 atoms)									
Max.	0.11	0.19	0.53	63.82	0.22	40.83	0.07	0.32	102.53	0.011	0.008	1.097	1.111	0.028	1.988	0.004	0.001	0.006	2.005	
Min.	0.04	0.00	<dl	59.35	<dl	37.37	<dl	<dl	100.53	0.005	0.002	0.984	0.995	-	1.886	-	-	-	1.886	
SD	0.02	0.05	0.11	1.49	0.04	1.12	0.01	0.09	0.69	0.002	0.002	0.037	0.038	0.009	0.032	0.001	0.000	0.001	0.038	
Mean	0.07	0.08	0.36	62.93	0.10	38.20	0.02	0.07	101.73	0.007	0.003	1.008	1.019	0.014	1.964	0.002	-	0.001	1.981	
	Hessite (sample 374, n = 4)										Formula (to 3 atoms)									
Max.	0.20	0.26	<dl	64.14	0.22	37.91	0.07	0.34	102.82	0.021	0.011	0.991	1.016	-	2.000	0.004	0.001	0.006	2.007	
Min.	0.12	0.12	<dl	63.36	0.12	36.23	<dl	<dl	100.38	0.012	0.005	0.967	0.993	-	1.978	0.002	-	-	1.984	
SD	0.03	0.06	-	0.28	0.04	0.69	0.00	0.07	0.93	0.003	0.003	0.010	0.010	-	0.011	0.001	0.000	0.002	0.010	
Mean	0.16	0.19	<dl	63.75	0.15	37.19	0.02	0.18	101.64	0.017	0.008	0.981	1.005	-	1.989	0.003	0.000	0.003	1.995	

Note: <dl, below minimum limit of detection. For detailed data, see Table S4.

EPMA data for tetradymite are listed in Table 5. Tetradymite is stoichiometric Bi_{1.93}Te_{1.92}S_{1.01}Se_{0.13} (15 data) with detectable Cu (0.08 wt.%), Ag (0.06 wt.%), Cd (0.04 wt.%), and Pb (0.05 wt.%). The ratios of Bi/(Te+Se+S) for Zhibula tetradymite are 0.62–0.65, as plotted in Figure 6f. We note the presence of 0.74–2.17 wt.% Se in Zhibula tetradymite.

Silver–(Au) tellurides are dominated by hessite (Table 6). Analysis of hessite gives the formula Ag_{1.97}Te_{1.00}S_{0.01}Se_{0.01} (n = 11). Traces of Cu (average 0.17 wt.%), Hg (average 0.12 wt.%), Bi (average 0.02 wt.%), Se (average 0.12 wt.%), and Au (average 0.11 wt.%) are noted. Despite its relative abundance in the samples, the fine grain size of petzite prohibited acquisition of high-quality compositional data.

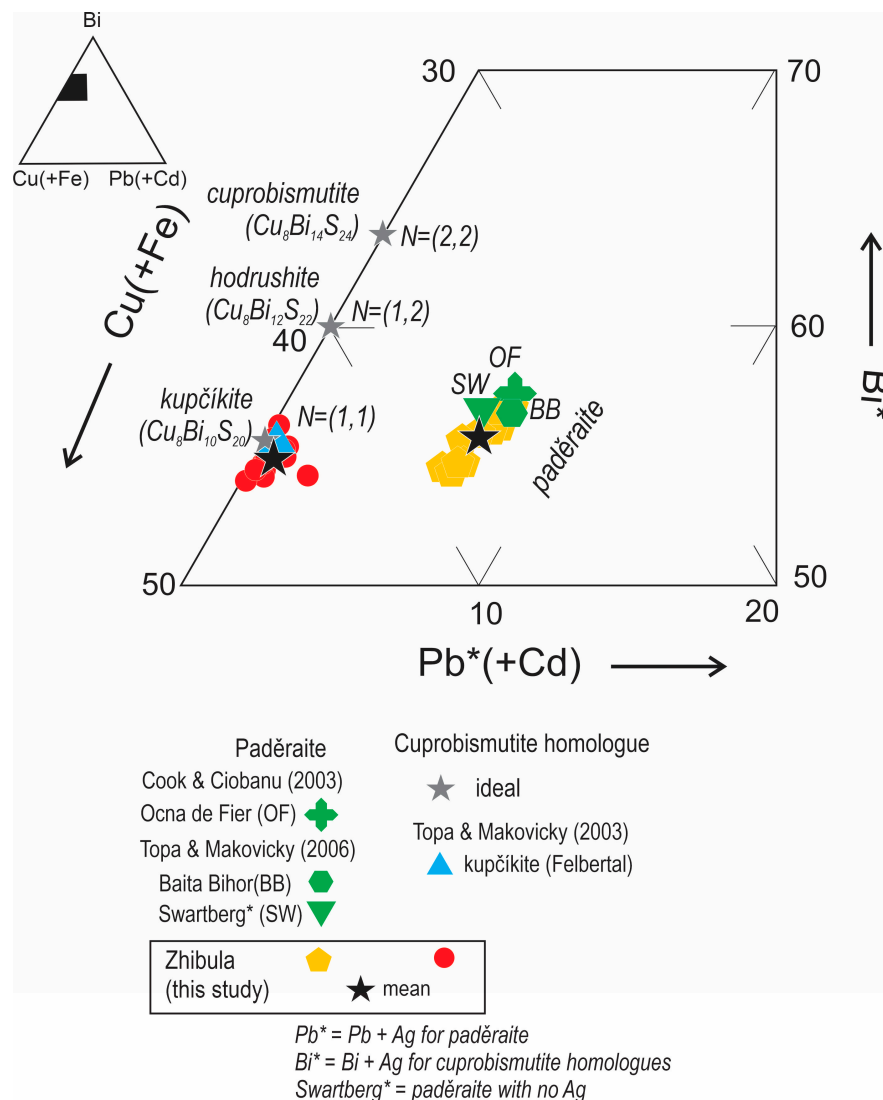


Figure 9. Ternary Cu(+Fe)—Bi*—Pb*(+Cd) plot for cuprobismutite homologues and padéraitite (after [9]) showing the composition of Zhibula specimens. Data of padéraitite are from [9,25], and kupčikite are from [8].

Carrollite associated with bornite contains 12.16–18.18 wt.% Cu, 26.07–36.24 wt.% Co, 9.91–11.25 wt.% Ni, and 0.05–4.07 wt.% Fe, giving the calculated formula $\text{Cu}_{0.59-0.90}\text{Fe}_{0.00-0.23}\text{Co}_{1.39-1.88}\text{Ni}_{0.52-0.60}\text{S}_{3.97-4.02}$ (Table S5). Analyzed grains also contain measurable concentrations of Bi (0.10–0.17 wt.%), Te (0.02–0.07 wt.%), and Se (<dl~0.08 wt.%).

Pyrrhotite contains measurable Ni (mean 0.83 wt.%) and Co (mean 0.14 wt.%) (Table S6). Pyrrhotite is non-stoichiometric and has a generic formula of Fe_{1-x}S ($0 < x < 0.125$; e.g., [26]). The x value of Zhibula pyrrhotite averages 0.108. Exsolved pentlandite in pyrrhotite has low Fe (mean 35.23 wt.%) and high Ni (mean 26.94 wt.%) with a mean formula of $\text{Fe}_{4.86}\text{Ni}_{3.54}\text{Co}_{0.35}\text{S}_{8.23}$. Pentlandite contains minor Co (1.30–3.22 wt.%), Se (0.05–0.09 wt.%), and negligible Te (<dl~0.03 wt.%).

Galena contains significant concentrations of Ag (mean 1.14 wt.%) and Bi (mean 2.31 wt.%), as well as detectable Se (mean 0.20 wt.%), Cu (mean 0.25 wt.%), Te (mean 0.05 wt.%), and Cd (mean 0.05 wt.%) (Table S7). Small grain size hampered efforts to obtain reliable compositional data for seleniferous galena (galena–clausthalite solid solution; Figure 3e).

Two markedly different types of sphalerite are observed (Table S7). The first (in sample 321) is characterized by high Fe (average 12.59 wt.%) and Cd (average 1.34 wt.%), low Zn

(average 51.24 wt.%), and measurable average contents of Co (0.08 wt.%) and Ni (0.05 wt.%). The second features low Fe (mean 1.24 wt.%) and Cd (mean 0.22 wt.%), high Zn (mean 64.01 wt.%), with detectable Co (mean 0.26 wt.%), traces of In (mean 0.02 wt.%), and Hg (mean 0.05 wt.%), but without detectable Ni.

4.3.2. LA-ICP-MS Trace Element Data

In an attempt to corroborate the concentrations of elements of interest in common sulfides, trace element analysis by LA-ICP-MS was undertaken on selected grains of chalcopyrite and bornite (Table S8).

Bornite from two samples confirms the notable enrichment in Bi (846–27,467 ppm, average 7351 ppm), Ag (264–901 ppm, average 462 ppm), Se (143–543 ppm, average 302 ppm), and Te (3.0–283 ppm, average 63 ppm). Two samples (374 and 8) display distinct Bi and Se contents (Figure 10a,b). Additionally, a positive correlation between Ag and Te is noted (Figure 10c).

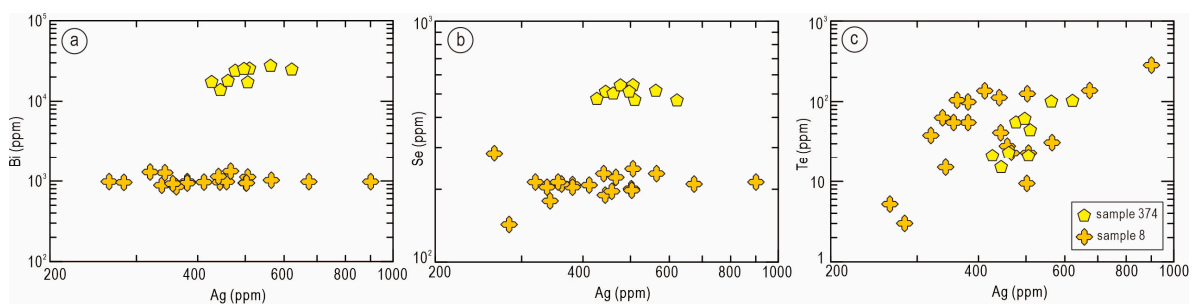


Figure 10. Binary plots of Ag vs. Bi (a), Ag vs. Se (b), and Ag vs. Te (c) in bornite.

In comparison, chalcopyrite shows much lower concentrations of Bi (<dl~75 ppm, average 8.8 ppm), Ag (0.17–14 ppm, average 2.8 ppm), Te (0.31–5.0 ppm, average 1.8 ppm), and Se (90–234 ppm, average 139 ppm). We note, however, higher In concentrations in chalcopyrite (1.7–6.3 ppm) than in bornite (0.03–3.3 ppm).

5. Discussion

5.1. A New Skarn Occurrence of Kupčikite and Padëraite, the First Report from China

The present study introduces a new occurrence of kupčikite and padëraite, minerals that are for the first time reported from a Chinese locality. Kupčikite is a member of the cuprobismutite homologous series of copper–bismuth sulfosalts [8,14]. Padëraite is not a member of the cuprobismutite homologous series, but is chemically and structurally related to it [6,9,25,27]. Structural relationships between padëraite and the cuprobismutite homologous series were postulated by Mumme [27], and later illustrated as nanoscale intergrowths between padëraite and cuprobismutite in Ciobanu et al. [6]. Cook and Ciobanu [9] postulated that padëraite belonged to a closely related homologous series with potential links to cuprobismutite series via the substitution $\text{Cu} + \text{Bi} \rightarrow 2\text{Pb}$. Topa and Makovicky [25] discussed hypothetical intergrowths between padëraite and cuprobismutite homologues.

The cuprobismutite homologous series, $\text{Cu}_8\text{Me}_{4(N-1)+2}^{(\text{quasi})\text{oct}}\text{Bi}_8^{\text{sq.pyr}}\text{S}_{4N+16}$, (oct = octahedral; sq. pyr. = square pyramidal; where Me = Bi, Ag, Fe; [5,14]) comprises three named minerals with layered structures and predictable compositional variation via the homologue number $N = (N_1 + N_2)/2$; N_1 and N_2 relate to the incremental quasi-octahedral layer. Kupčikite, $\text{Cu}_{3.4}\text{Fe}_{0.6}\text{Bi}_5\text{S}_{10}$, was first described from type locality (TL), the Felbertal scheelite deposit, Hohe Tauern, Austria [8] and is the simplest $N = (1,1)$ homologue (Figure 9). This corresponds structurally to the synthetic phase $\text{Cu}_4\text{Bi}_5\text{S}_{10}$ of Mariolacos [28]. It differs, however, from the synthetic equivalent in that it also contains Fe, an element that seems to be essential for mineral stability in the geological environment. Kupčikite contains more Fe than other cuprobismutite homologues, but typically only minor Ag or Cd, if any. Compositional data for kupčikite from black shale-hosted hydrothermal Ni-

Bi-As mineralization at Čierna Lehota, Slovakia show a significant Pb content (2.73 wt.%), yielding the formula $(\text{Cu}_{3.92}\text{Fe}_{0.24}\text{Bi}_{4.60}\text{Pb}_{0.19}\text{Ag}_{0.04}\text{Sb}_{0.01}\text{S}_{9.58})$ [11]. Kupčikite from granitic pegmatites in Karkonosze Massif, southwestern Poland has traces of Zn (~0.20 wt.%) $(\text{Cu}_{6.67}\text{Fe}_{1.22}\text{Zn}_{0.10}\text{Bi}_{9.99}\text{S}_{20.03})$ [12]. The Zhibuka kupčikite is stoichiometric with Fe content (Fe = 0.59 apfu), comparable to the TL specimen, but also contains Se (0.14 apfu).

Paděraite was first described by Mumme and Žák [7] from Băița Bihor (Romania) with the empirical composition $\text{Cu}_{5.9}\text{Ag}_{1.3}\text{Pb}_{1.6}\text{Bi}_{11.2}\text{S}_{22}$. Mumme [27] proposed the structural formula $\text{Cu}_6\text{AgPbBi}_{12}\text{S}_{22}$. Paděraites from Swartberg (South Africa) and Ocna de Fier (Romania) yield different empirical formulae: $\text{Cu}_{7.36}\text{Pb}_{1.31}\text{Bi}_{11.32}\text{S}_{22}$ and $\text{Cu}_{7.11}\text{Ag}_{0.36}\text{Pb}_{1.2}\text{Bi}_{11.28}\text{S}_{22.05}$, respectively [9,10]. Due to the different Cu and Ag contents, Topa and Makovicky [25] distinguished between Ag-bearing paděraite (Băița Bihor) and Ag-free, Cu-enriched paděraite (Swartberg). Their structural formula can be expressed as $\text{Cu}_7(\text{X}_{0.33}\text{Pb}_{1.33}\text{Bi}_{11.33})\Sigma_{13}\text{S}_{22}$, where X is either Cu or Ag. Zhibula paděraite (Figure 9; Table 4) is also Ag-bearing, albeit with much lower Ag than the examples from Baita Bihor or Ocna de Fier, i.e., Ag = 0.09 apfu, compared to 0.2–0.3 and 0.3–0.4 apfu, respectively. It also contains relatively high content of Se (0.47 apfu) and minor Te (0.05 apfu). Notably, Zhibula paděraite differs from the other three specimens in that it contains Fe (0.34 apfu), an element that requires further constraints in terms of how it is incorporated into the crystal structure.

The interest in these rare minerals stems from the fact they are often intergrown with one another and with other Bi sulfosalts, particularly in skarn deposits rich in Bi minerals, such as those from Baita Bihor and Ocna de Fier [5,6,9,25]. In such skarn occurrences, the two minerals are enclosed within members of the bismuthinite derivative series, either aikinite or bismuthinite, respectively. Co-crystallization between cuprobismutite homologues is supported by micron and nanoscale intergrowths observed at Ocna de Fier [6,9], whereas Topa and Makovicky [25] propose replacement of hodrushite by paděraite in the Baita Bihor example.

The Zhibula skarn is outstanding in that kupčikite and paděraite, although associated, do not display such lamellar intergrowths with one another at either the micron- or nanoscale (Figures 7 and 8). Secondly, they are not associated with one of the bismuthinite derivatives (only aikinite is present at Zhibula), but instead co-crystallize with tetradymite (Figure 7a). Superimposed overprinting is evidenced by the observed replacement of wittichenite (Figure 7c) and reshaping of mutual phase boundaries (scalloped and ragged morphologies; Figure 7b,d). This implies that kupčikite and paděraite can be attributed to the prograde (diopside–andradite) skarn stage rather than the retrograde skarn stage (hedenbergite–johannsenite) in proximal skarn from Zhibula. Temperatures in the range 400–600 °C were constrained from phase associations for this stage and are corroborated by fluid inclusion data for the Zhibula skarn (405–667 °C; [22]). Likewise, the Ocna de Fier skarn records temperatures of 400–600 °C and ~371 °C during prograde and retrograde stages, respectively, as estimated from skarn associations [29].

Although few studies have mentioned the formation environments of Cu-Bi sulfosalts and associated paděraite, we note their occurrence is generally in deposits characterized by relatively high temperatures, including metamorphosed W deposits [8], granite-related Cu-rich veinlets, and Li-Be-bearing granitic pegmatite at Swartberg ([10] and references therein). Furthermore, based on fluid inclusion data (310–390 °C) for quartz from the Obari mine, Japan, formation of cuprobismutite-group minerals took place above 300 °C [13].

5.2. Genetic Constraints—Trace Minerals and Metallogenic Implications

Exotic trace mineralogy comprising Bi-Te-Au associations are typical of many deposits [3] and are common in skarn deposits of various types [30]. In the latter case, skarn orefield zonation can lead to specific ore assemblages, for example, as observed at Ocna de Fier [29,31]. This is also the case of the Zhibula skarn where proximal and distal skarn differ in terms of skarn mineralogy [23] and can be enriched in a range of exotic trace minerals, also including the W-Mo associations in the distal skarn reported by Xu et al. [24].

Mineralogical variability within calcic skarn deposits is an intrinsic characteristic of metasomatism driving the interaction between magma-derived fluids and carbonaceous protoliths ([29] and references therein). Therefore, skarn mineral associations will vary as a function of different protoliths, fluid components, and physicochemical conditions (X_{CO_2} , T, P, pH, etc.) (e.g., [32–34]). Similarly, ore mineral assemblages and accompanying trace mineral signatures are also likely to exhibit variation in different skarns. Based on prior results, including the work of Xu et al. [23], we here address the diversity of mineralization styles observed at Zhibula and discuss the local environments represented by the three distinct types of skarn ores.

The results presented here show that the proximal skarns (garnet- and pyroxene-dominant) host distinct ore and trace mineral associations. They both share Cu sulfides and trace Bi-Te minerals, although of different speciation. The distal skarn has its own distinct characteristics. The schematic in Figure 11 shows the formation of the three associations, “A1”, “A2” and “A3,” interpreted in terms of evolving f_{Te_2} – f_{S_2} conditions.

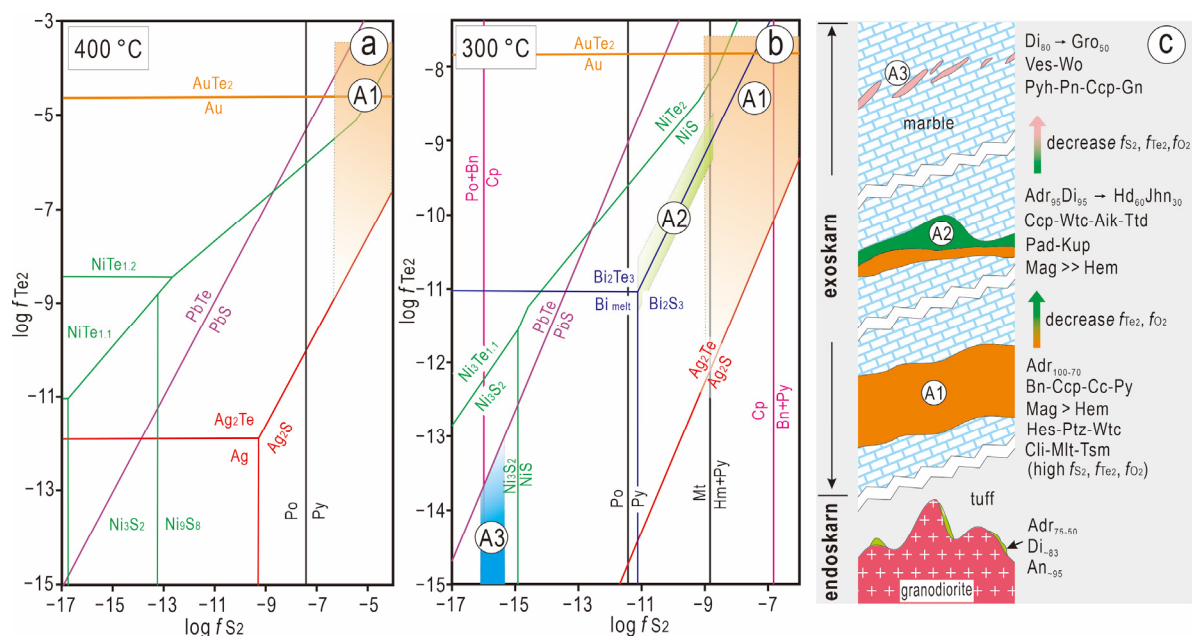


Figure 11. Stability diagrams in terms of $\log f_{\text{S}_2}$ and $\log f_{\text{Te}_2}$ for telluride and sulfide species at 400 °C and 300 °C, respectively (modified after [2,35]), and on the right, a cartoon illustrating three different mineral assemblages (A1, A2, and A3) and their evolution within the Zhibula Cu skarn. Abbreviations: Aik—aikinite; An—anorthite; Adr—andradite; Bn—bornite; Cli—carrollite; Ccp—chalcopyrite; Di—diopside; Gro—grossular; Gn—galena; Hed—hedenbergite; Hem—hematite; Hes—hessite; Jhn—johannsenite; Kup—kupčikite; Mag—magnetite; Mlt—melonite; Pde—padëraite; Pn—pentlandite; Ptz—petzite; Pyh—pyrrhotite; Tsm—tsumoite; Ttd—tetradymite; Ves—vesuvianite; Wtc—wittichenite; Wo—wollastonite.

5.2.1. Au-Ag Telluride Associations in Bornite–Chalcopyrite Ores

A first association “A1” (column in Figure 11) comprises bornite and chalcopyrite with minor carrollite, chalcocite, wittichenite, molybdenite, several tellurides (tsumoite, melonite, hessite, and petzite), and electrum (Figures 2b,c, 4 and 5). This is constrained at relatively high T, at least 400 °C, from conditions interpreted for host proximal garnet skarn [22] and f_{O_2} – f_{S_2} stability within the magnetite–pyrite field. Considering phase stabilities for tellurides from Afifi et al. [2], the field for association “A1” at 400 °C is constrained from the stability fields of Au tellurides versus that of native gold, as well as Ag and Ni telluride versus sulfide, and the presence of galena instead of altaite (Figure 11a). Overall, the co-existing mineral assemblage “A1,” consisting of bornite chalcopyrite, petzite–hessite,

magnetite–hematite, and wittichenite, suggests that they formed at relatively high f_{Te_2} , f_{S_2} , and f_{O_2} conditions (Figures 4 and 11) [35].

Trace element signatures and textural relationships between Cu-Fe sulfides and co-existing species further assist in characterizing association “A1.” Bornite has long been reported to accommodate Bi (~0.20 wt.%) and Ag (0.2–2.0 wt.%) (e.g., [36–38]). In Zhibula, bornite carries comparable concentrations of Bi (1021–21,419 ppm) and Ag (264–901 ppm), consistent with a hypogene origin and analogous to other comparable occurrences. Bismuth and Se, particularly the Bi in bornite, display two distinct groups (Figure 10a,b), probably indicating the variation in formation temperatures, as higher Bi incorporation into bornite occurs under elevated temperatures. Considering the intergrowth textures among bornite, chalcopyrite, wittichenite, and hessite (Figures 4 and 5), they probably represent a hypogene assemblage formed during the early high-temperature prograde skarn stage. Carrollite is likely also part of this stage, whereas chalcocite and galena are attributable to the retrograde stage (Figure 4a–c).

The unusual Bi-rich bornite-like phase (average 6.73 wt.%) observed in minor amounts at Zhibula stands out against the “normal” low-Bi (0.20 wt.%) variety (Figure 4d–f). Similar textures are reported from the Yangzhaiyu Au deposit, China, in which the brighter patches in bornite contain up to 7.7 wt.% Bi [39]. These findings are, however, in agreement with the experimental work of Sugaki et al. [40], which showed that bornite occupies a relatively extensive field of solid solution at higher temperatures and can incorporate as much as 17.2 wt.% Bi at 420 °C and 11.4 wt.% Bi at 300 °C. Moreover, Nanri et al. [41] reported that bornite solid solution can reach a maximum of 18.2 wt.% Bi at 500 °C. The observations are also consistent with fluid inclusion data from co-existing quartz (250–420 °C, mean ~300 °C) [22]. The mechanism by which the two compositionally distinct bornites co-exist is, however, unclear at present, and may possibly reflect unmixing of two distinct bornite superstructures during cooling.

5.2.2. Bismuth Sulfosalt and Tellurides in Magnetite–Chalcopyrite Ore Prograde to Retrograde Skarn Transition

Minor and trace minerals comprising Cu-Bi sulfosalts (wittichenite, aikinite, kupčikite, and padëraite), and tetradymite (Figures 6 and 7), hereafter called assemblage “A2” (column in Figure 11), are hosted within magnetite–chalcopyrite ore recording lower temperatures and a reducing event from higher to lower f_{O_2} , from diopside–andradite to hedenbergite–johannsenite skarn (Figure 2d–h; [23]). Such an overprint is also expressed by a coarsening of the Bi minerals within zoned garnet or new growth within magnetite, from mottled chalcopyrite cores to marginal inclusions of Bi minerals (Figure 2f,g). Coarsening of Bi minerals is also accommodated along mutual boundaries between magnetite and chalcopyrite (e.g., the tetradymite in Figure 2g). We note the presence of Se in tetradymite (0.74–2.17 wt.%), as well as kupčikite and padëraite.

Assemblage “A2” is shown within a narrow stability field formed at lower temperature (~300 °C) and f_{Te_2} (disappearance of Au-Ag tellurides and all other tellurides except tetradymite), but higher f_{S_2} than assemblage “A1” (Figure 11b). Nonetheless, as discussed above, early padëraite and kupčikite could have formed during prograde formation of diopside–andradite skarn at ~400 °C.

5.2.3. Pyrrhotite–Chalcopyrite in Distal Skarn

A further reducing skarn assemblage comprising grossular garnet, vesuvianite, wolastonite, and anorthite, which hosts pyrrhotite and chalcopyrite [23], hereafter called association “A3” (Figure 11b), is represented by the distal skarn. Association “A3” is estimated to form at the lowest f_{O_2} , f_{S_2} , and f_{Te_2} conditions. Exsolution of lamellar pentlandite from pyrrhotite is apparently favored by cooling from high temperatures (e.g., [42]), so we used a temperature of 300 °C for the phase diagram shown in Figure 11b).

Although the mineral assemblages are different in each of the three skarn types, the primary fluids and their sources are likely to be the same. For example, Co and Ni

crystallize as carrollite and melonite in bornite–chalcopyrite ores from andradite skarn, but are instead incorporated into high Co- and Ni-bearing pyrrhotite (mean 0.83 wt.% and 0.14 wt.%, respectively) and pyrrhotite (<dl~0.15 wt.% Co and 0.63–0.91 wt.% Ni) in the distal (banded grossular) skarn.

In summary, the complex and varied ore mineral assemblages observed in the Zhibula Cu skarn (Bi-bearing bornite, Au-Ag tellurides, Cu-Bi sulfosalts, Bi chalcogenides, Co-Ni sulfides, and scheelite–powellite) reflect a complex magmatic–hydrothermal system, closely related to the nearby Qulong porphyry Cu-Mo deposit [22–24]. The Zhibula deposit has a characteristic metallogenic signature (Cu, Au, Ag, Te, Se, Bi, Co, W, and Mo). These elements are common accessories in base metal skarns and occur within a variety of mineral assemblages depending on the prevailing wall rocks and local physicochemical conditions. Mineralogical investigation that is sufficiently detailed to establish the mode of occurrence of minor minerals and their contained elements of interest is not only helpful to indicate how the ore was formed and evolved but also provides fundamental information necessary to achieve recovery and optimal beneficiation of these critical metals as by-products.

6. Summary and Conclusions

The Zhibula \pm Cu skarn contains a group of conspicuous trace ore minerals, including high Bi-bearing bornite (average 6.73 wt.%), Cu-Bi sulfosalts (wittichenite, aikinite, kupčikite, and paděraite), Au-Ag tellurides (hessite, petzite), and Bi chalcogenides (tetradymite). During a decrease in temperature from 400 °C to 300 °C, the stability fields for these Au and Ag tellurides changed and f_{Te_2} was reduced, which can be clearly noted by phase equilibrium between AuTe_2 and gold. Similarly, $\log f_{\text{S}_2}$ decreases from -7.4 to -11.4 , as marked by the relative prevalence of pyrrhotite relative to pyrite. Overall, the co-existing mineral assemblage “A1,” consisting of bornite–chalcopyrite, petzite–hessite, magnetite (\pm hematite), and wittichenite, suggests that they formed in relatively high f_{Te_2} , f_{S_2} , and f_{O_2} conditions. In contrast, the abundant Bi-Te associations in magnetite–chalcopyrite ore (association “A2”) have formed during the retrograde sulfidation of pyroxene-dominant skarn at lower f_{Te_2} and higher f_{S_2} .

Kupčikite $(\text{Cu}_{3.43}\text{Fe}_{0.59})_{4.02}(\text{Bi}_{4.96}\text{Pb}_{0.02}\text{Cd}_{0.03}\text{Ag}_{0.01})_{5.02}(\text{S}_{9.82}\text{Se}_{0.14})_{9.96}$ and paděraite $(\text{Cu}_7(\text{Cu}_{0.05}\text{Ag}_{0.09}\text{Fe}_{0.34}\text{Pb}_{1.31}\text{Cd}_{0.02}\text{Bi}_{11.10})_{12.91}(\text{S}_{21.56}\text{Se}_{0.47}\text{Te}_{0.05})_{22.08}$ from Zhibula skarn do not form nanoscale intergrowths with one another.

The most reduced assemblage is chalcopyrite and pyrrhotite within the distal skarn at the contact with marble (association “A3”). Cobalt and nickel occur as discrete minerals: cobaltite, melonite, and pentlandite. The precious metal association is restricted to bornite–chalcopyrite ores.

These trace ore mineral signatures (assemblages, their compositions and mutual textures) suggest precipitation from a high-temperature magmatic–hydrothermal system. Together with the skarn assemblages, trace ore mineralogy supports a genetic relationship with the nearby Qulong porphyry Cu-Mo deposit and represents evidence for an evolution of the ore-forming fluids from high f_{S_2} – f_{Te_2} conditions, through a moderate S-fugacity, towards relatively reduced, lower f_{S_2} , f_{O_2} , and f_{Te_2} conditions. The observed evolution also corresponds to a diverse suite of local environments controlled by lithology and structure.

Supplementary Materials: The following are available online at <https://www.mdpi.com/article/10.3390/min14050474/s1>. Supplementary Material: A (EPMA and LA-ICP-MS methodology), Tables S1–S7 (complete EPMA datasets) and Table S8 (LA-ICP-MS trace element dataset).

Author Contributions: J.X. and C.L.C. conceived this contribution and conducted all analytical work. The manuscript was written by J.X., N.J.C. and C.L.C., with contributions from S.G., T.Z. and J.J. All authors have read and agreed to the published version of the manuscript.

Funding: J.X. acknowledges support from the National Natural Science Foundation of China (grant 42230807; 92162217).

Data Availability Statement: Data are contained within the article and Supplementary Materials.

Acknowledgments: We thank Benjamin Wade, Ashley Slattery and Sarah Gilbert (Adelaide Microscopy) for their kind assistance with instrument operation. J.X. expresses appreciation to Youye Zheng for his assistance with fieldwork. Constructive comments from two anonymous reviewers assisted us to clarify aspects of presentation and expression.

Conflicts of Interest: The authors declare no conflicts of interest.

References

1. Xie, G.Q.; Li, X.H.; Han, Y.X.; Zhu, Q.Q.; Li, W.; Ye, H.; Song, S.W. Recent progress in study of enrichment mechanism of tellurium, selenium and thallium from oxidized gold-rich porphyry-skarn deposits. *Miner. Depos.* **2020**, *39*, 559–567. (In Chinese with English Abstract)
2. Afifi, A.M.; Kelly, W.C.; Essene, E.J. Phase relations among tellurides, sulfides, and oxides; Pt. II, applications to telluride-bearing ore deposits. *Econ. Geol.* **1988**, *83*, 395–404. [[CrossRef](#)]
3. Cook, N.; Ciobanu, C. Bismuth tellurides and sulphosalts from the Larga hydrothermal system, Metaliferi Mts, Romania: Paragenesis and genetic significance. *Mineral. Mag.* **2004**, *68*, 301–321. [[CrossRef](#)]
4. Ciobanu, C.L.; Cook, N.J.; Pring, A. Bismuth tellurides as gold scavengers. In Proceedings of the Mineral Deposit Research: Meeting the Global Challenge: Proceedings of the Eighth Biennial SGA Meeting, Beijing, China, 18–21 August 2005; Mao, J.W., Bierlein, F.P., Eds.; Springer: Berlin/Heidelberg, Germany, 2005; pp. 1383–1386.
5. Topa, D.; Makovicky, E.; Balić-Žunić, T. Crystal structures and crystal chemistry of members of the cuprobismutite homologous series of sulfosalts. *Can. Mineral.* **2003**, *41*, 1481–1501. [[CrossRef](#)]
6. Ciobanu, C.L.; Pring, A.; Cook, N.J. Micron-to nano-scale intergrowths among members of the cuprobismutite series and padëraite: HRTEM and microanalytical evidence. *Mineral. Mag.* **2004**, *68*, 279–300. [[CrossRef](#)]
7. Mumme, W.G.; Žák, L.P. $\text{Cu}_{5.9}\text{Ag}_{1.3}\text{Pb}_{1.6}\text{Bi}_{11.2}\text{S}_{22}$, a new mineral of the cuprobismutite-hodrushite group. *Neues Jahrb. Mineral. Monatsh.* **1985**, *12*, 557–567.
8. Topa, D.; Makovicky, E.; Balic-Zunic, T.; Paar, W.H. Kupcikite, $\text{Cu}_{3.4}\text{Fe}_{0.6}\text{Bi}_5\text{S}_{10}$, a new Cu-Bi sulfosalts from, Felbertal, Austria, and its crystal structure, Locality: Felbertal, Austria. *Can. Mineral.* **2003**, *41*, 1155–1166. [[CrossRef](#)]
9. Cook, N.J.; Ciobanu, C.L. Lamellar minerals of the cuprobismutite series and related padëraite: A new occurrence and implications. *Can. Mineral.* **2003**, *41*, 441–456. [[CrossRef](#)]
10. Ciobanu, C.L.; Cook, N.J.; Topa, D.; Bogdanov, K.; Merkle, R.K.W. Compositional variance in the cuprobismutite series and related (Pb-bearing) padëraite: Insights from new occurrences. In Proceedings of the 18th General Meeting, Edinburgh, UK, 1–6 September 2002; p. 264.
11. Pršek, J.; Mikus, T.; Makovicky, E.; Chovan, M. Cuprobismutite, kupcikite, hodrushite and associated sulfosalts from the black shale hosted Ni-Bi-As mineralization at Cierna Lehota, Slovakia. *Eur. J. Mineral.* **2005**, *17*, 155–162. [[CrossRef](#)]
12. Pieczka, A.; Gołëbiowska, B. Cuprobismutite homologues in granitic pegmatites from Szklarska Poręba, Karkonosze Massif, southwestern Poland. *Can. Mineral.* **2012**, *50*, 313–324. [[CrossRef](#)]
13. Izumino, Y.; Nakashima, K.; Nagashima, M. Cuprobismutite group minerals (cuprobismutite, hodrushite, kupcikite and padëraite), other Bi-sulfosalts and Bi-tellurides from the Obari mine, Yamagata Prefecture, Japan. *J. Mineral. Petrol. Sci.* **2014**, *109*, 177–190. [[CrossRef](#)]
14. Makovicky, E. Modular classification of sulphosalts: Current status, definition and application of homologous series. *Neues Jahrb. Mineral. Abh.* **1989**, *160*, 269–297.
15. Hou, Z.Q.; Duan, L.F.; Lu, Y.J.; Zheng, Y.C.; Zhu, D.C.; Yang, Z.M.; Yang, Z.S.; Wang, B.D.; Pei, Y.R.; Zhao, Z.D. Lithospheric architecture of the Lhasa Terrane and its control on ore deposits in the Himalayan-Tibetan Orogen. *Econ. Geol.* **2015**, *110*, 1541–1575. [[CrossRef](#)]
16. Hou, Z.Q.; Yang, Z.M.; Lu, Y.J.; Kemp, A.; Zheng, Y.C.; Li, Q.Y.; Tang, J.X.; Yang, Z.S.; Duan, L.F. A genetic linkage between subduction-and collision-related porphyry Cu deposits in continental collision zones. *Geology* **2015**, *43*, 247–250. [[CrossRef](#)]
17. Wang, S.; Cao, M.J.; Li, G.M.; Evans, N.J.; Silang, W.D.; Qin, K.Z. Tracing the genesis of the Zhibula skarn deposit, Tibet, using Co, Te, Au and Ag occurrence. *Ore Geol. Rev.* **2023**, *160*, 105601. [[CrossRef](#)]
18. Wang, S.; Cao, M.J.; Li, G.M.; Shan, P.F.; Qin, K.Z. The occurrence of cobalt and implications for genesis of the Pusangguo cobalt-rich skarn deposit in Gangdese, Tibet. *Ore Geol. Rev.* **2022**, *150*, 105193. [[CrossRef](#)]
19. Dong, Y.H.; Xu, J.F.; Zeng, Q.G.; Mao, G.Z.; Li, J. Is there a Neo-Tethys' subduction record earlier than arc volcanic rocks in the Sangri group? *Acta Petrol. Sin.* **2006**, *22*, 661–668, (In Chinese with English Abstract).
20. Hu, Y.B.; Liu, J.Q.; Ling, M.X.; Ding, W.; Liu, Y.; Zartman, R.E.; Sun, W.D. The formation of Qulong adakites and their relationship with porphyry copper deposit: Geochemical constraints. *Lithos* **2015**, *220*, 60–80. [[CrossRef](#)]
21. Li, G.M.; Rui, Z.Y.; Wang, G.M.; Lin, F.C.; Liu, B.; She, H.Q.; Feng, C.Y.; Qu, W.J. Molybdenite Re-Os dating of Jiama and Zhibula polymetallic copper deposits in Gangdese metallogenic belt of Tibet and its significance. *Mineral. Depos.* **2005**, *24*, 481–489. (In Chinese with English Abstract)
22. Xu, J.; Zheng, Y.Y.; Sun, X.; Shen, Y.H. Alteration and mineralization at the Zhibula Cu skarn deposit, Gangdese belt, Tibet. *Ore Geol. Rev.* **2016**, *75*, 304–326. [[CrossRef](#)]

23. Xu, J.; Ciobanu, C.L.; Cook, N.J.; Zheng, Y.Y.; Sun, X.; Wade, B.P. Skarn formation and trace elements in garnet and associated minerals from Zhibula copper deposit, Gangdese Belt, southern Tibet. *Lithos* **2016**, *262*, 213–231. [[CrossRef](#)]
24. Xu, J.; Ciobanu, C.L.; Cook, N.J.; Slattery, A. Crystals from the powellite-scheelite series at the nanoscale: A case study from the Zhibula Cu skarn, Gangdese Belt, Tibet. *Minerals* **2019**, *9*, 340. [[CrossRef](#)]
25. Topa, D.; Makovicky, E. The crystal structure of paderaitite, $\text{Cu}_7(\text{X}_{0.33}\text{Pb}_{1.33}\text{Bi}_{11.33})\Sigma_{13}\text{S}_{22}$, with X = Cu or Ag: New data and interpretation. *Can. Mineral.* **2006**, *44*, 481–495. [[CrossRef](#)]
26. Becker, M.; Bradshaw, D.; De Villiers, J. The mineralogy of pyrrhotite from Sudbury CCN and Phoenix nickel ores and its effect on flotation performance. *Can. Metal. Quart.* **2011**, *50*, 10–19. [[CrossRef](#)]
27. Mumme, W.G. The crystal structure of padëraite, a mineral of the cuprobismutite series. *Can. Mineral.* **1986**, *24*, 513–521.
28. Mariolacos, K. Phase relations in the system $\text{Bi}_2\text{S}_3\text{-PbS-CuPbBiS}_3$ at 450 °C and its extension in the system $\text{Bi}_2\text{S}_3\text{-PbS-Cu}_2\text{S}$. *Neues Jahrb. Mineral. Monatsh.* **1979**, *13*, 73–80.
29. Ciobanu, C.L.; Cook, N.J. Skarn textures: A case study of the Ocna de Fier-Dognecea orefield, Banat, Romania. *Ore Geol. Rev.* **2004**, *24*, 315–370. [[CrossRef](#)]
30. Meinert, L.D. Gold in skarns related to epizonal intrusions. *Rev. Econ. Geol.* **2000**, *13*, 347–375.
31. Cook, N.J.; Ciobanu, C.L. Paragenesis of Cu-Fe ores from Ocna de Fier-Dognecea (Romania), typifying fluid plume mineralization in a proximal skarn setting. *Mineral. Mag.* **2001**, *65*, 351–372. [[CrossRef](#)]
32. Bowman, J.R. Basic aspects and applications of phase equilibria in the analysis of metasomatic Ca-Mg-Al-Fe-Si skarns. In *Mineralized Intrusion Related Skarn Systems*; Lentz, D.R., Ed.; Mineralogical Association of Canada Short Course; Mineralogical Association of Canada: Ottawa, ON, Canada, 1998; Volume 26, pp. 1–49.
33. Meinert, L.D. Skarns and skarn deposits. *Geosci. Can. Repr. Ser.* **1992**, *6*, 117–134.
34. Dipple, G.M.; Gerdes, M.L. Reaction-infiltration feedback and hydrodynamics at the skarn front. In *Mineralized Intrusion-Related Skarn Systems*; Lentz, D.R., Ed.; Mineralogical Association of Canada Short Course; Mineralogical Association of Canada: Ottawa, ON, Canada, 1998; Volume 26, pp. 71–97.
35. Mueller, A.G.; Hagemann, S.G.; Jol, B.; Yanlu, X.; Roberts, M.P. Early Fimiston and late Oroya Au-Te ore, Paringa south mine, golden mile, Kalgoorlie: 4. Mineralogical and thermodynamic constraints on gold deposition by magmatic fluids at 420–300 °C and 300 Mpa. *Mineral. Depos.* **2020**, *55*, 767–796. [[CrossRef](#)]
36. Oen, I.S.; Kieft, C. Silver-bearing wittichenite-chalcopyrite-bornite intergrowths and associated minerals in the Mangualade pegmatite, Portugal. *Can. Mineral.* **1976**, *14*, 185–193.
37. Shalaby, I.M.; Stumpfl, E.; Helmy, H.M.; El Mahallawi, M.M.; Kamel, O.A. Silver and silver-bearing minerals at the Um Samiuki volcanogenic massive sulphide deposit, Eastern Desert, Egypt. *Mineral. Depos.* **2004**, *39*, 608–621. [[CrossRef](#)]
38. Novoselov, K.A.; Belogub, E.V.; Zaykov, V.V.; Yakovlev, V.A. Silver sulfosalts from volcanic-hosted massive sulphide deposits in the Southern Urals. *Mineral. Petrol.* **2006**, *87*, 327–349. [[CrossRef](#)]
39. Jian, W.; Lehmann, B.; Mao, J.; Ye, H.; Li, Z.; Zhang, J.; Ye, Y. Telluride and Bi-sulfosalts mineralogy of the Yangzhaiyu gold deposit, Xiaoqinling region, Central China. *Can. Mineral.* **2014**, *52*, 883–898. [[CrossRef](#)]
40. Sugaki, A.; Kitakaze, A.; Harada, H. Hydrothermal synthesis and phase relations of the polymetallic sulfide system, especially on the Cu-Fe-Bi-S system. In *Materials Science of the Earth's Interior*; Sunagawa, I., Ed.; Terra Publication: Tokyo, Japan, 1984; pp. 545–583.
41. Nanri, H.; Sugaki, A.; Shima, H.; Kitakaze, A. Phase relations of Cu-Fe-Bi-S system (V) bornite solid solution field at 400 °C and 500 °C (abstr.). *J. Jpn. Assoc. Miner. Petrol. Econ. Geol.* **1978**, *73*, 83. (In Japanese)
42. Dobbe, R.T.M.; Oen, I.S. The polymetallic Cu-Co ores in the central mineralised zone at Tunaberg, Bergslagen, Sweden. *Neues Jahrb. Mineral. Abh.* **1994**, *166*, 261–294.

Disclaimer/Publisher's Note: The statements, opinions and data contained in all publications are solely those of the individual author(s) and contributor(s) and not of MDPI and/or the editor(s). MDPI and/or the editor(s) disclaim responsibility for any injury to people or property resulting from any ideas, methods, instructions or products referred to in the content.